3
Crystal Interfaces and Microstructure

Basically three different types of interface are important in metallic systems:

1. The free surfaces of a crystal (solid/vapour interface)
2. Grain boundaries (α/α interfaces)
3. Interphase interfaces (α/β interfaces).

All crystals possess the first type of interface. The second type separates crystals with essentially the same composition and crystal structure, but a different orientation in space. The third interface separates two different phases that can have different crystal structures and/or compositions and therefore also includes solid/liquid interfaces.

The great majority of phase transformations in metals occur by the growth of a new phase (β) from a few nucleation sites within the parent phase (α)—a nucleation and growth process. The α/β interface therefore plays an important role in determining the kinetics of phase transformations and is the most important class of interface listed. It is, however, also the most complex and least understood, and this chapter thus begins by first considering the simpler interfaces, (1) and (2).

The solid/vapour interface is of course itself important in vaporization and condensation transformations, while grain boundaries are important in recrystallization, i.e. the transformation of a highly deformed grain structure into new undeformed grains. Although no new phase is involved in recrystallization it does have many features in common with phase transformations.

The importance of interfaces is not restricted to what can be called the primary transformation. Since interfaces are an almost essential feature of the transformed microstructure, a second (slower) stage of most transformations is the microstructural coarsening that occurs with time[1]. This is precisely analogous to the grain coarsening or grain growth that follows a recrystallization transformation.

3.1 Interfacial Free Energy

It is common practice to talk of interfacial energy. In reality, however, what is usually meant and measured by experiment is the interfacial free energy, γ. The free energy of a system containing an interface of area A and free energy

γ per unit area is given by

$$G = G_0 + A\gamma \tag{3.1}$$

where G_0 is the free energy of the system assuming that all material in the system has the properties of the bulk—γ is therefore the *excess* free energy arising from the fact that some material lies in or close to the interface. It is also the work that must be done at constant T and P to create unit area of interface.

Consider for simplicity a wire frame suspending a liquid film, Fig. 3.1. If one bar of the frame is movable it is found that a force F per unit length must be applied to maintain the bar in position. If this force moves a small distance so that the total area of the film is increased by dA the work done by the force is $F dA$. This work is used to increase the free energy of the system by dG. From Equation 3.1

$$dG = \gamma dA + A d\gamma$$

Equating this with $F dA$ gives

$$F = \gamma + A\frac{d\gamma}{dA} \tag{3.2}$$

In the case of a liquid film the surface energy is independent of the area of the interface and $d\gamma/dA = 0$. This leads to the well-known result

$$F = \gamma \tag{3.3}$$

i.e. a surface with a free energy γ J m^{-2} exerts a surface tension of γ N m^{-1}.

In the case of interfaces involving *solids*, however, it is not immediately obvious that γ is independent of area. Since a liquid is unable to support shear stresses, the atoms within the liquid can rearrange during the stretching process and thereby maintain a constant surface structure. Solids, however, are much more viscous and the transfer of atoms from the bulk to the surface, which is necessary to maintain an unchanged surface structure and energy, will take much longer. If this time is long in comparison to the time of the experiment then $d\gamma/dA \neq 0$ and surface free energy and surface tension will not be identical. Nevertheless, at temperatures near the melting point the atomic mobility is usually high enough for Equation 3.3 to be applicable.

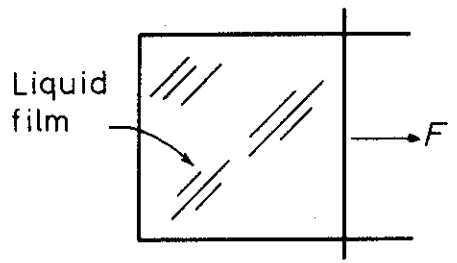

Fig. 3.1 A liquid film on a wire frame.

3.2 Solid/Vapour Interfaces

To a first approximation the structure of solid surfaces can be discussed in terms of a hard sphere model. If the surface is parallel to a low-index crystal plane the atomic arrangement will be the same as in the bulk, apart from perhaps a small change in lattice parameter. (This assumes that the surface is uncontaminated: in real systems surfaces will reduce their free energies by the adsorption of impurities.) Figure 3.2 for example shows the {111} {200} {220} atom planes in the fcc metals. Note how the density of atoms in these planes decreases as $(h^2 + k^2 + l^2)$ increases. (The notation {200} and {220} has been used instead of {100} and {110} because the spacing of equivalent atom planes is then given by $a/\sqrt{(h^2 + k^2 + l^2)}$ where a is the lattice parameter.)

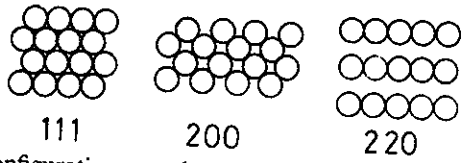

Fig. 3.2 Atomic configurations on the three closest-packed planes in fcc crystals: (111), (200) and (220).

The origin of the surface free energy is that atoms in the layers nearest the surface are without some of their neighbours. Considering only nearest neighbours it can be seen that the atoms on a {111} surface, for example, are deprived of three of their twelve neighbours. If the bond strength of the metal is ε each bond can be considered as lowering the internal energy of each atom by $\varepsilon/2$. Therefore every surface atom with three 'broken bonds' has an excess internal energy of $3\varepsilon/2$ over that of the atoms in the bulk. For a pure metal ε can be estimated from the heat of sublimation L_s. (The latent heat of sublimation is equal to the sum of the latent heat of melting (or fusion) and the latent heat of vaporization.) If 1 mol of solid is vaporized 12 N_a broken bonds are formed. Therefore $L_s = 12\ N_a\ \varepsilon/2$. Consequently the energy of a {111} surface should be given by

$$E_{sv} = 0.25\ L_s/N_a \quad \text{J/surface atom} \tag{3.4}$$

This result will only be approximate since second nearest neighbours have been ignored and it has also been assumed that the strengths of the remaining bonds in the surface are unchanged from the bulk values.

From the definition of Gibbs free energy the surface free energy will be given by

$$\gamma = E + PV - TS \tag{3.5}$$

Thus even if the 'PV' term is ignored surface entropy effects must be taken into account. It might be expected that the surface atoms will have more freedom of movement and therefore a higher thermal entropy compared to

atoms in the bulk. Extra configurational entropy can also be introduced into the surface by the formation of surface vacancies for example. The surface of a crystal should therefore be associated with a positive excess entropy which will partly compensate for the high internal energy of Equation 3.4.

Experimental determination of γ_{sv} is difficult[2] but the measured values for pure metals indicate that near the melting temperature the surface free energy averaged over many surface planes is given by

$$\gamma_{sv} = 0.15\ L_s/N_a \quad \text{J/surface atom} \tag{3.6}$$

As a result of entropy effects γ_{sv} is slightly dependent on temperature. From Equation 1.10

$$\left(\frac{\partial \gamma}{\partial T}\right)_P = -S \tag{3.7}$$

Measured values of S are positive and vary between 0 and 3 mJ m^{-2} K^{-1}. Some selected values of γ_{sv} at the melting point are listed in Table 3.1. Note that metals with high melting temperatures have high values for L_s and high surface energies.

Table 3.1 Average Surface Free Energies of Selected Metals

Values selected from H. Jones 'The surface energy of solid metals', *Metal Science Journal*, **5**:15 (1971). Experimental errors are generally about 10%. The values have been extrapolated to the melting temperature, T_m.

Crystal	T_m/°C	γ_{sv}/mJ m^{-2}
Sn	232	680
Al	660	1080
Ag	961	1120
Au	1063	1390
Cu	1084	1720
δ-Fe	1536	2080
Pt	1769	2280
W	3407	2650

It can be seen from the above simple model that different crystal surfaces should have different values for E_{sv} depending on the number of broken bonds (see exercise 3.1). A little consideration will show that for the surfaces shown in Fig. 3.2 the number of broken bonds at the surface will increase through the series {111} {200} {220}. Therefore ignoring possible differences in the entropy terms γ_{sv} should also increase along the same series.

When the macroscopic surface plane has a high or irrational {*hkl*} index the surface will appear as a stepped layer structure where each layer is a close-packed plane. This is illustrated for a simple cubic crystal in Fig. 3.3.

3.2 Solid/Vapour Interfaces

To a first approximation the structure of solid surfaces can be discussed in terms of a hard sphere model. If the surface is parallel to a low-index crystal plane the atomic arrangement will be the same as in the bulk, apart from perhaps a small change in lattice parameter. (This assumes that the surface is uncontaminated: in real systems surfaces will reduce their free energies by the adsorption of impurities.) Figure 3.2 for example shows the {111} {200} {220} atom planes in the fcc metals. Note how the density of atoms in these planes decreases as $(h^2 + k^2 + l^2)$ increases. (The notation {200} and {220} has been used instead of {100} and {110} because the spacing of equivalent atom planes is then given by $a/\sqrt{(h^2 + k^2 + l^2)}$ where a is the lattice parameter.)

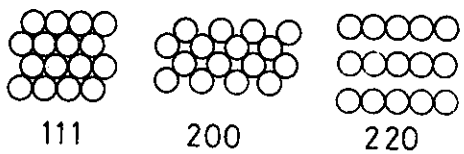

Fig. 3.2 Atomic configurations on the three closest-packed planes in fcc crystals: (111), (200) and (220).

The origin of the surface free energy is that atoms in the layers nearest the surface are without some of their neighbours. Considering only nearest neighbours it can be seen that the atoms on a {111} surface, for example, are deprived of three of their twelve neighbours. If the bond strength of the metal is ε each bond can be considered as lowering the internal energy of each atom by $\varepsilon/2$. Therefore every surface atom with three 'broken bonds' has an excess internal energy of $3\varepsilon/2$ over that of the atoms in the bulk. For a pure metal ε can be estimated from the heat of sublimation L_s. (The latent heat of sublimation is equal to the sum of the latent heat of melting (or fusion) and the latent heat of vaporization.) If 1 mol of solid is vaporized 12 N_a broken bonds are formed. Therefore $L_s = 12\ N_a\ \varepsilon/2$. Consequently the energy of a {111} surface should be given by

$$E_{sv} = 0.25\ L_s/N_a \quad \text{J/surface atom} \tag{3.4}$$

This result will only be approximate since second nearest neighbours have been ignored and it has also been assumed that the strengths of the remaining bonds in the surface are unchanged from the bulk values.

From the definition of Gibbs free energy the surface free energy will be given by

$$\gamma = E + PV - TS \tag{3.5}$$

Thus even if the 'PV' term is ignored surface entropy effects must be taken into account. It might be expected that the surface atoms will have more freedom of movement and therefore a higher thermal entropy compared to

atoms in the bulk. Extra configurational entropy can also be introduced into the surface by the formation of surface vacancies for example. The surface of a crystal should therefore be associated with a positive excess entropy which will partly compensate for the high internal energy of Equation 3.4.

Experimental determination of γ_{sv} is difficult[2] but the measured values for pure metals indicate that near the melting temperature the surface free energy averaged over many surface planes is given by

$$\gamma_{sv} = 0.15\ L_s/N_a \quad \text{J/surface atom} \tag{3.6}$$

As a result of entropy effects γ_{sv} is slightly dependent on temperature. From Equation 1.10

$$\left(\frac{\partial \gamma}{\partial T}\right)_P = -S \tag{3.7}$$

Measured values of S are positive and vary between 0 and 3 mJ m^{-2} K^{-1}. Some selected values of γ_{sv} at the melting point are listed in Table 3.1. Note that metals with high melting temperatures have high values for L_s and high surface energies.

Table 3.1 Average Surface Free Energies of Selected Metals

Values selected from H. Jones 'The surface energy of solid metals', *Metal Science Journal*, **5**:15 (1971). Experimental errors are generally about 10%. The values have been extrapolated to the melting temperature, T_m.

Crystal	T_m/°C	γ_{sv}/mJ m^{-2}
Sn	232	680
Al	660	1080
Ag	961	1120
Au	1063	1390
Cu	1084	1720
δ-Fe	1536	2080
Pt	1769	2280
W	3407	2650

It can be seen from the above simple model that different crystal surfaces should have different values for E_{sv} depending on the number of broken bonds (see exercise 3.1). A little consideration will show that for the surfaces shown in Fig. 3.2 the number of broken bonds at the surface will increase through the series {111} {200} {220}. Therefore ignoring possible differences in the entropy terms γ_{sv} should also increase along the same series.

When the macroscopic surface plane has a high or irrational {*hkl*} index the surface will appear as a stepped layer structure where each layer is a close-packed plane. This is illustrated for a simple cubic crystal in Fig. 3.3.

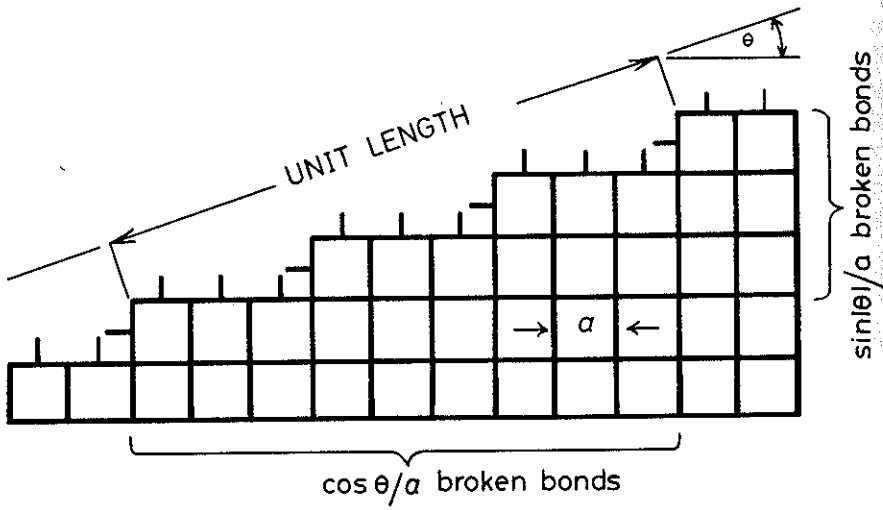

Fig. 3.3 The 'broken-bond' model for surface energy.

A crystal plane at an angle θ to the close-packed plane will contain broken bonds in excess of the close-packed plane due to the atoms at the steps. For unit length of interface in the plane of the diagram and unit length out of the paper (parallel to the steps) there will be $(\cos\theta/a)(1/a)$ broken bonds out of the close-packed plane and $(\sin|\theta|/a)(1/a)$ additional broken bonds from the atoms on the steps. Again attributing $\varepsilon/2$ energy to each broken bond, then

$$E_{sv} = (\cos\theta + \sin|\theta|)\varepsilon/2a^2 \qquad (3.8)$$

This is plotted as a function of θ in Fig. 3.4. Note that the close-packed orientation ($\theta = 0$) lies at a cusped minimum in the energy plot. Similar arguments can be applied to any crystal structure for rotations about any axis from any reasonably close-packed plane. All low-index planes should therefore be located at low-energy cusps.

If γ is plotted v. θ similar cusps are found, but as a result of entropy effects

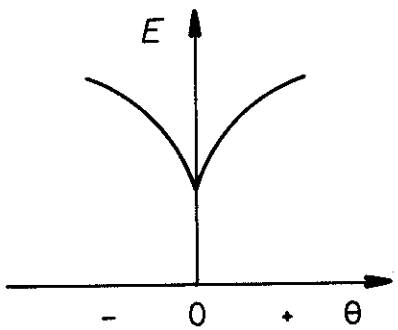

Fig. 3.4 Variation of surface energy as a function of θ in Fig. 3.3.

they are less prominent than in the E–θ plot, and for the higher index planes they can even disappear.

A convenient method for plotting the variation of γ with surface orientation in three dimensions is to construct a surface about an origin such that the free energy of any plane is equal to the distance between the surface and the origin when measured along the normal to the plane in question. A section through such a surface is shown in Fig. 3.5a. This type of polar representation of γ is known as a γ-plot and has the useful property of being able to predict the equilibrium shape of an isolated single crystal.

For an isolated crystal bounded by several planes A_1, A_2, etc. with energies γ_1, γ_2, etc. the total surface energy will be given by the sum $A_1\gamma_1 + A_2\gamma_2 + \cdots$ The equilibrium shape has the property that $\Sigma A_i\gamma_i$ is a minimum and the shape that satisfies this condition is given by the following, so-called *Wulff* construction[3]. For every point on the γ surface, such as A in Fig. 3.5a, a plane is drawn through the point and normal to the radius vector

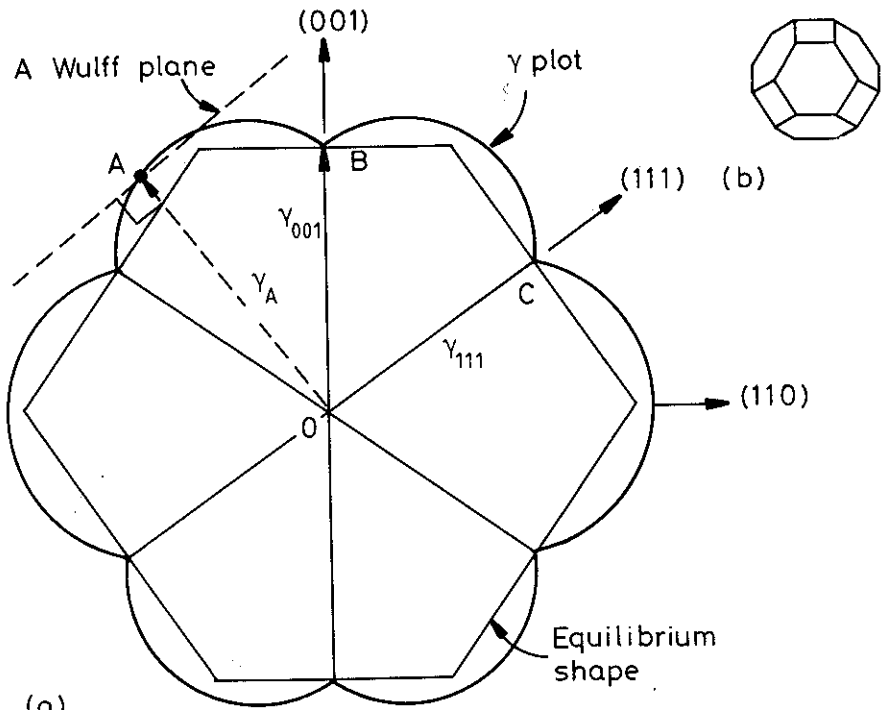

Fig. 3.5 (a) A possible $(1\bar{1}0)$ section through the γ-plot of an fcc crystal. The length OA represents the free energy of a surface plane whose normal lies in the direction OA. Thus $OB = \gamma_{(001)}$, $OC = \gamma_{(111)}$, etc. Wulff planes are those such as that which lies normal to the vector OA. In this case the Wulff planes at the cusps (B, C, etc.) give the inner envelope of all Wulff planes and thus the equilibrium shape. (b) The equilibrium shape in three dimensions showing {100} (square faces) and {111} (hexagonal faces).

OA. The equilibrium shape is then simply the inner envelope of all such planes. Therefore when the γ-plot contains sharp cusps the equilibrium shape is a polyhedron with the largest facets having the lowest interfacial free energy.

Equilibrium shapes can be determined experimentally by annealing small single crystals at high temperatures in an inert atmosphere, or by annealing small voids inside a crystal[4]. Fcc crystals for example usually assume a form showing {100} and {111} facets as shown in Fig. 3.5b. Of course when γ is isotropic, as for liquid droplets, both the γ-plot and equilibrium shapes are spheres.

When the equilibrium shape is known it is possible to use the Wulff theorem in reverse to give the relative interfacial free energies of the observed facet planes. In Fig. 3.5 for example the widths of the crystal in the ⟨111⟩ and ⟨100⟩ directions will be in the ratio of $\gamma(111):\gamma(100)$. {110} facets are usually missing from the equilibrium shape of fcc metals, but do however appear for bcc metals[5].

The aim of this section has been to show, using the simplest type of interface, the origin of interfacial free energy, and to show some of the methods available for estimating this energy. Let us now consider the second type of interface, grain boundaries.

3.3 Boundaries in Single-Phase Solids

The grains in a single-phase polycrystalline specimen are generally in many different orientations and many different types of grain boundary are therefore possible. The nature of any given boundary depends on the misorientation of the two adjoining grains and the orientation of the boundary plane relative to them. The lattices of any two grains can be made to coincide by rotating one of them through a suitable angle about a *single* axis. In general the axis of rotation will not be simply oriented with respect to either grain or the grain-boundary plane, but there are two special types of boundary that are relatively simple. These are pure tilt boundaries and pure twist boundaries, as illustrated in Fig. 3.6. A tilt boundary occurs when the axis of rotation is parallel to the plane of the boundary, Fig. 3.6a, whereas a twist boundary is formed when the rotation axis is perpendicular to the boundary, Fig. 3.6b.

3.3.1 *Low-Angle and High-Angle Boundaries*

It is simplest to first consider what happens when the misorientation between two grains is small. This type of boundary can be simply considered as an array of dislocations. Two idealized boundaries are illustrated in Fig. 3.7. These are symmetrical *low-angle tilt* and *low-angle twist* boundaries. The

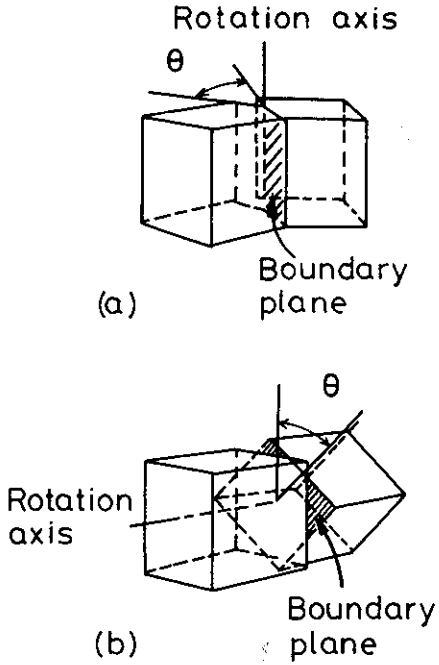

Fig. 3.6 The relative orientations of the crystals and the boundary forming (a) a tilt boundary (b) a twist boundary.

low-angle tilt boundary is an array of parallel edge dislocations, whereas the twist boundary is a cross-grid of two sets of screw dislocations. In each case the atoms in the regions between the dislocations fit almost perfectly into both adjoining crystals whereas the dislocation cores are regions of poor fit in which the crystal structure is highly distorted.

The tilt boundary need not be symmetrical with respect to the two adjoining crystals. However, if the boundary is unsymmetrical dislocations with different Burgers vectors are required to accommodate the misfit, as illustrated in Fig. 3.8. In general boundaries can be a mixture of the tilt and twist type in which case they must contain several sets of different edge and screw dislocations.

The energy of a low-angle grain boundary is simply the total energy of the dislocations within unit area of boundary. (For brevity the distinction between internal energy and free energy will usually not be made from now on except where essential to understanding.) This depends on the spacing of the dislocations which, for the simple arrays in Fig. 3.7, is given by

$$D = \frac{b}{\sin\theta} \simeq \frac{b}{\theta} \tag{3.9}$$

where b is the Burgers vector of the dislocations and θ is the angular misorientation across the boundary. At very small values of θ the dislocation

spacing is very large and the grain boundary energy γ is approximately proportional to the density of dislocations in the boundary $(1/D)$, i.e.

$$\gamma \propto \theta \tag{3.10}$$

However as θ increases the strain fields of the dislocations progressively cancel out so that γ increases at a decreasing rate as shown in Fig. 3.9. In general when θ exceeds 10–15° the dislocation spacing is so small that the dislocation cores overlap and it is then impossible to physically identify the individual dislocations (see Fig. 3.10). At this stage the grain-boundary energy is almost independent of misorientation, Fig. 3.9.

When $\theta > 10$–15° the boundary is known as a *random high-angle grain boundary*. The difference in structure between low-angle and high-angle grain boundaries is lucidly illustrated by the bubble-raft model in Fig. 3.11. High-angle boundaries contain large areas of poor fit and have a relatively open structure. The bonds between the atoms are broken or highly distorted and consequently the boundary is associated with a relatively high energy. In

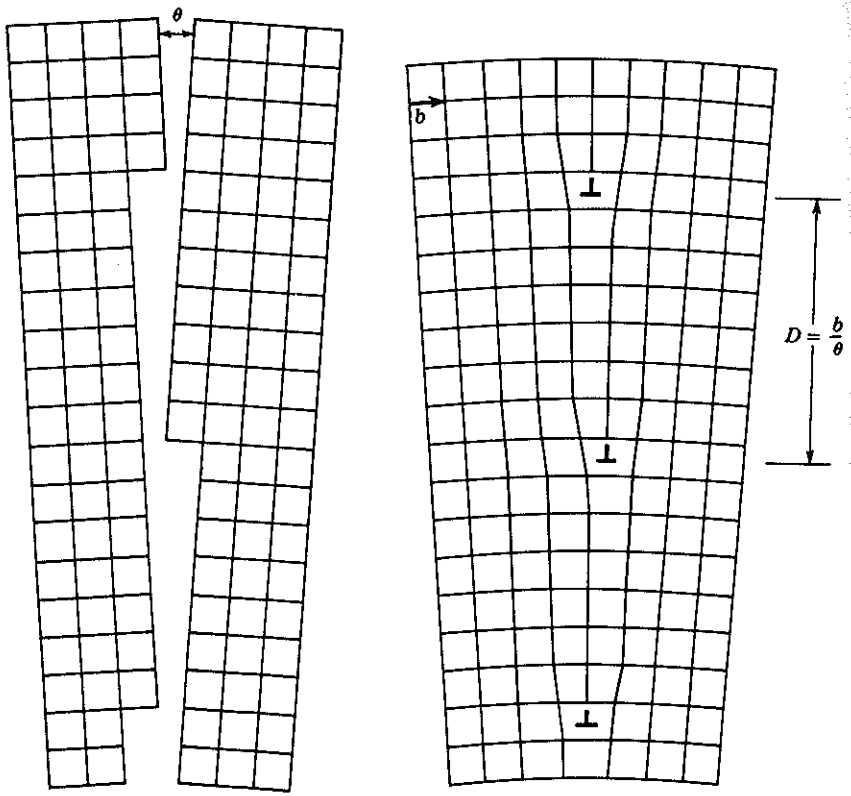

(a)

Fig. 3.7 (a) Low-angle tilt boundary, (b) low-angle twist boundary: ○ atoms in crystal below boundary, ● atoms in crystal above boundary. (After W.T. Read Jr., *Dislocations in Crystals*, McGraw-Hill, New York, 1953.)

low-angle boundaries, however, most of the atoms fit very well into both lattices so that there is very little free volume and the interatomic bonds are only slightly distorted. The regions of poor fit are restricted to the dislocation cores which are associated with a higher energy similar to that of the random high-angle boundary.

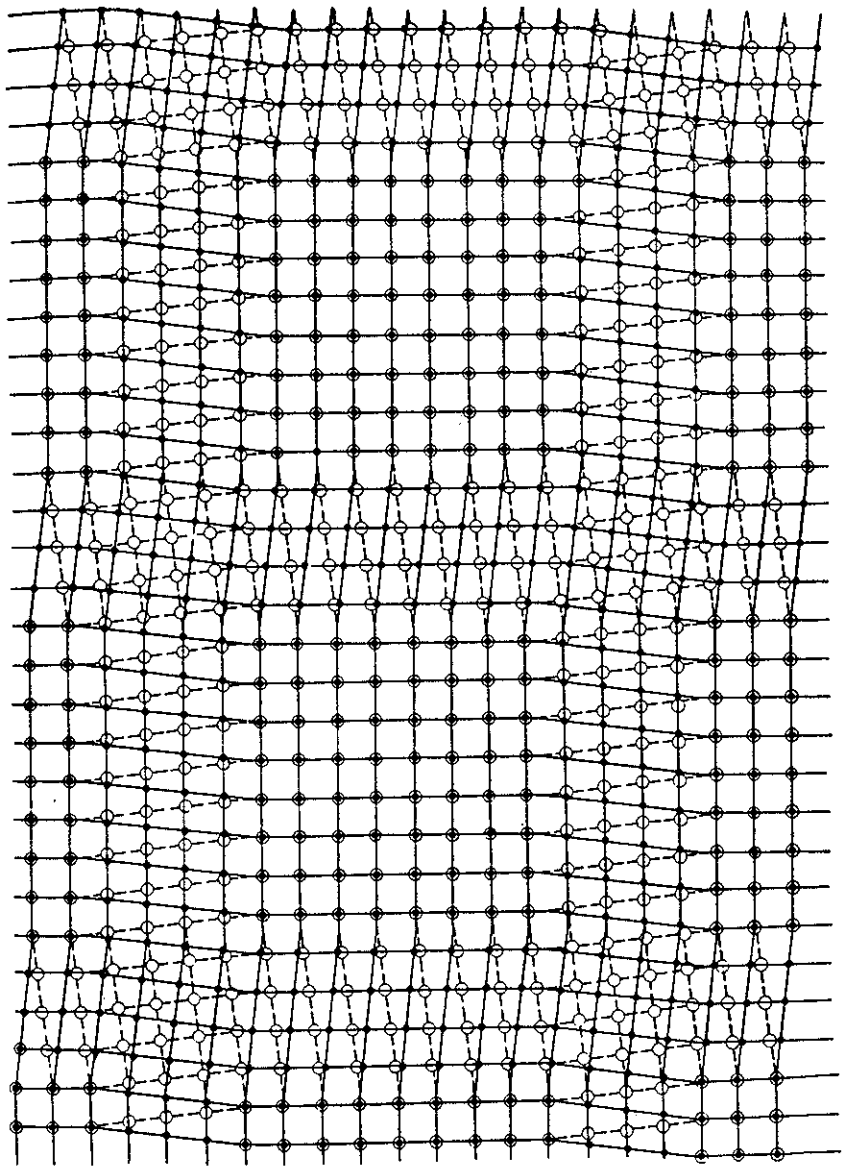

Fig. 3.7 (b)

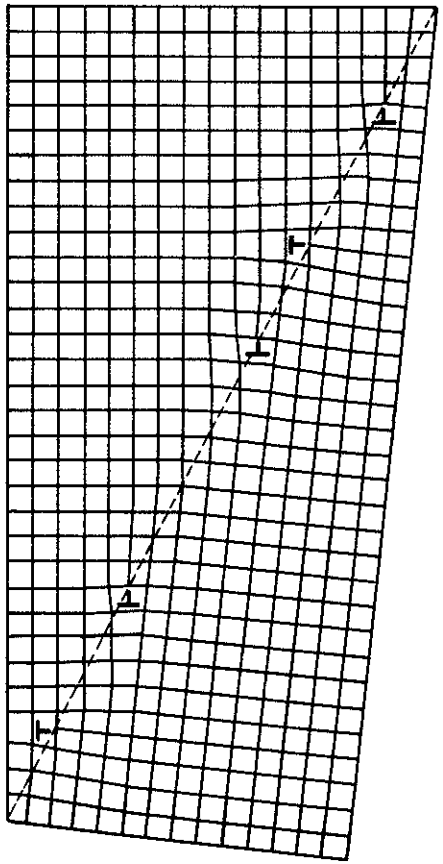

Fig. 3.8 An unsymmetric tilt boundary. Dislocations with two different Burgers vectors are present. (After W.T. Read Jr., *Dislocations in Crystals*, McGraw-Hill, New York, 1953.)

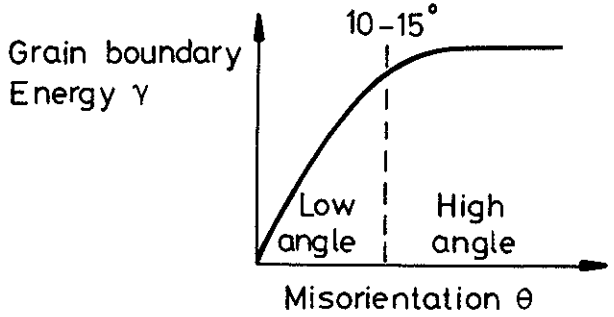

Fig. 3.9 Variation of grain boundary energy with misorientation (schematic).

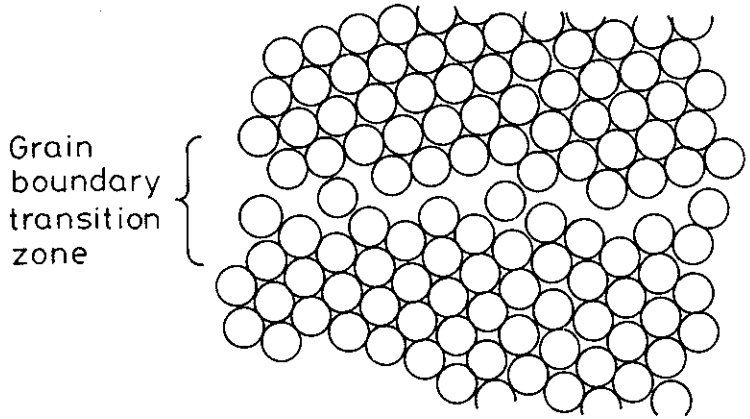

Fig. 3.10 Disordered grain boundary structure (schematic).

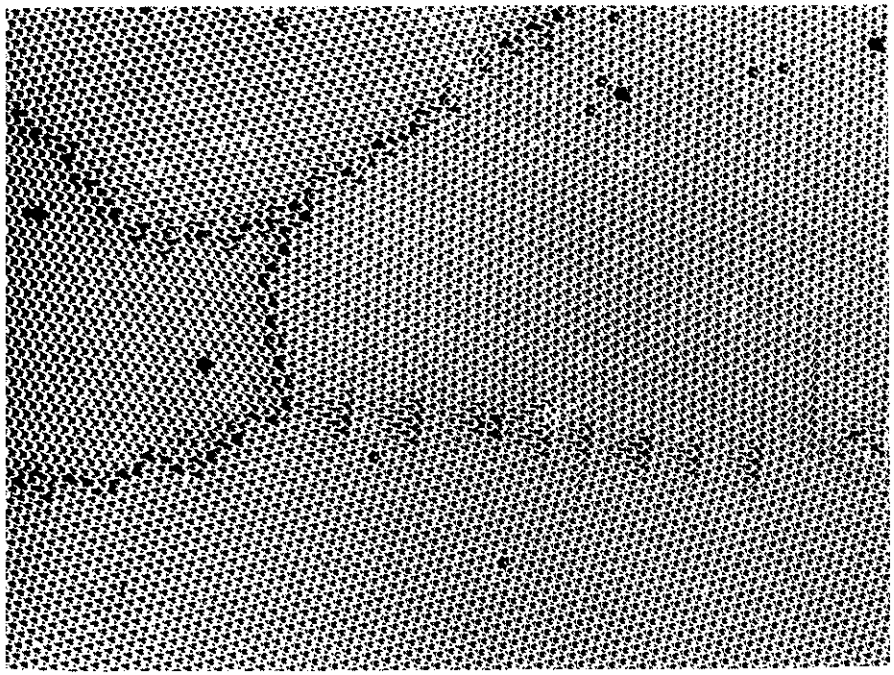

Fig. 3.11 Rafts of soap bubbles showing several grains of varying misorientation. Note that the boundary with the smallest misorientation is made up of a row of dislocations, whereas the high-angle boundaries have a disordered structure in which individual dislocations cannot be identified. (After P.G. Shewmon, *Transformations in Metals*, McGraw-Hill, New York, 1969, from C.S. Smith.)

Measured high-angle grain boundary energies γ_b are often found to be roughly given by

$$\gamma_b \simeq \frac{1}{3}\gamma_{sv} \tag{3.11}$$

Some selected values for γ_b and γ_b/γ_{sv} are listed in Table 3.2. As for surface energies γ_b is temperature dependent decreasing somewhat with increasing temperature.

Table 3.2 Measured Grain Boundary Free Energies

Values selected from compilation given in *Interfacial Phenomena in Metals and Alloys*, by L.E. Murr, Addison-Wesley, London, 1975.

Crystal	γ_b/mJ m^{-2}	T/°C	γ_b/γ_{sv}
Sn	164	223	0.24
Al	324	450	0.30
Ag	375	950	0.33
Au	378	1000	0.27
Cu	625	925	0.36
γ-Fe	756	1350	0.40
δ-Fe	468	1450	0.23
Pt	660	1300	0.29
W	1080	2000	0.41

3.3.2 *Special High-Angle Grain Boundaries*

Not all high-angle boundaries have an open disordered structure. There are some *special high-angle boundaries* which have significantly lower energies than the random boundaries. These boundaries only occur at particular misorientations and boundary planes which allow the two adjoining lattices to fit together with relatively little distortion of the interatomic bonds.

The simplest special high-angle grain boundary is the boundary between two twins. If the twin boundary is parallel to the twinning plane the atoms in the boundary fit perfectly into both grains. The result is a *coherent twin boundary* as illustrated in Fig. 3.12a. In fcc metals this is a {111} close-packed plane. Because the atoms in the boundary are essentially in undistorted positions the energy of a coherent twin boundary is extremely low in comparison to the energy of a random high-angle boundary.

If the twin boundary does not lie exactly parallel to the twinning plane, Fig. 3.12b, the atoms do not fit perfectly into each grain and the boundary energy is much higher. This is known as an *incoherent twin boundary*. The energy of a twin boundary is therefore very sensitive to the orientation of the

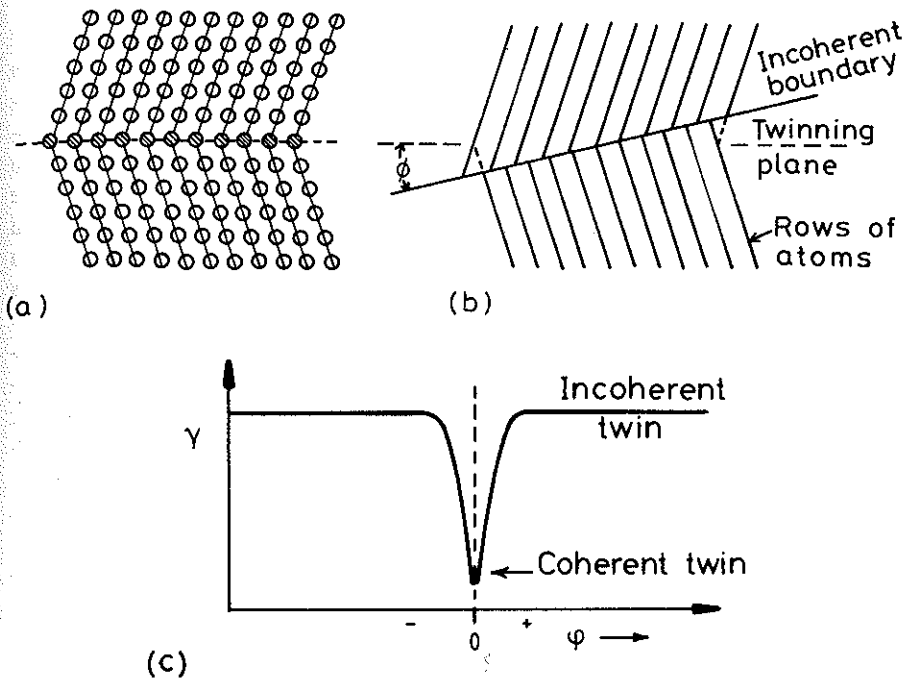

Fig. 3.12 (a) A coherent twin boundary. (b) An incoherent twin boundary. (c) Twin-boundary energy as a function of the grain boundary orientation.

boundary plane. If γ is plotted as a function of the boundary orientation a sharp cusped minimum is obtained at the coherent boundary position as shown in Fig. 3.12c. Table 3.3 lists some experimentally measured values of coherent and incoherent twins along with high-angle grain boundary energies for comparison.

Table 3.3 Measured Boundary Free Energies for Crystals in Twin Relationships (Units mJ m^{-2})

Values selected from compilation given in *Interfacial Phenomena in Metals and Alloys*, by L.E. Murr, Addison-Wesley, London, 1975.

Crystal	Coherent twin boundary energy	Incoherent twin boundary energy	Grain boundary energy
Cu	21	498	623
Ag	8	126	377
Fe-Cr-Ni (stainless steel type 304)	19	209	835

Twin orientations in fcc metals correspond to a misorientation of 70.5° about a ⟨110⟩ axis. Therefore a twin boundary is a special high-angle grain boundary, and a coherent twin boundary is a symmetrical tilt boundary between the two twin-related crystals. Figure 3.13 shows measured grain-boundary energies for various symmetric tilt boundaries in aluminium. When the two grains are related by a rotation about a ⟨100⟩ axis, Fig. 3.13a, it can be seen that most high-angle boundaries have about the same energy and should therefore have a relatively disordered structure characteristic of random boundaries. However, when the two grains are related by a rotation about a ⟨110⟩ axis there are several large-angle orientations which have significantly lower energies than the random boundaries (Fig. 3.13b). $\theta = 70.5°$ corresponds to the coherent twin boundary discussed above, but low-energy boundaries are also found for several other values of θ. The reasons for these other special grain boundaries are not well understood. However, it seems reasonable to suppose that the atomic structure of these boundaries is such that they contain extensive areas of good fit. A two-dimensional example is shown in Fig. 3.14. This is a symmetrical tilt boundary between grains with a misorientation of 38.2°. The boundary atoms fit rather well into both grains leaving relatively little free volume. Moreover, a small group of atoms (shaded) are repeated at regular intervals along the boundary.

3.3.3 *Equilibrium in Polycrystalline Materials*

Let us now examine how the possibility of different grain-boundary energies affects the microstructure of a polycrystalline material. Figure 3.15 shows the microstructure of an annealed austenitic stainless steel (fcc). The material contains high- and low-angle grain boundaries as well as coherent and incoherent twin boundaries. This microstructure is determined by how the different grain boundaries join together in space. When looking at two-

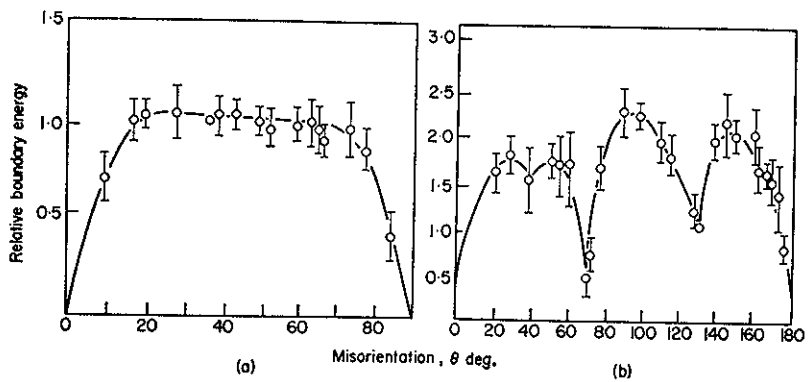

Fig. 3.13 Measured grain boundary energies for symmetric tilt boundaries in Al (a) when the rotation axis is parallel to ⟨100⟩, (b) when the rotation axis is parallel to ⟨110⟩. (After G. Hasson and C. Goux, *Scripta Metallurgica*, **5** (1971) 889.)

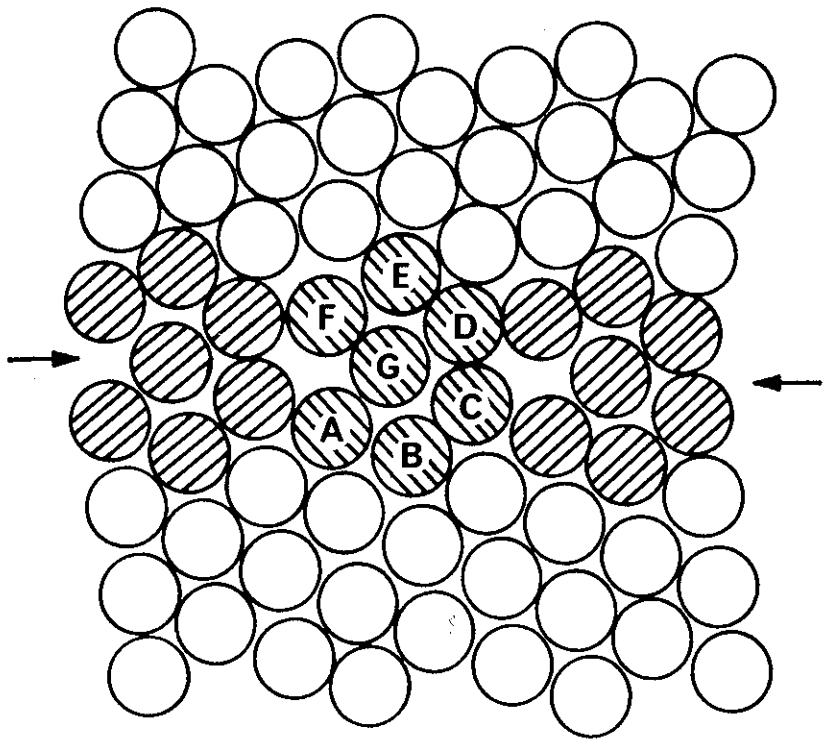

Fig. 3.14 Special grain boundary. (After H. Gleiter, *Physica Status Solidi* (b) **45** (1971) 9.)

dimensional microstructures like this it is important to remember that in reality the grains fill three dimensions, and only one section of the three-dimensional network of internal boundaries is apparent. Note that two grains meet in a plane (a grain boundary) three grains meet in a line (a grain edge) and four grains meet at a point (a grain corner). Let us now consider the factors that control the grain shapes in a recrystallized polycrystal.

The first problem to be solved is why grain boundaries exist at all in annealed materials. The boundaries are all high-energy regions that increase the free energy of a polycrystal relative to a single crystal. Therefore a polycrystalline material is never a true equilibrium structure. However the grain boundaries in a polycrystal can adjust themselves during annealing to produce a *metastable* equilibrium at the grain boundary intersections.

The conditions for equilibrium at a grain-boundary junction can be obtained either by considering the total grain boundary energy associated with a particular configuration or, more simply, by considering the forces that each boundary exerts on the junction. Let us first consider a grain-boundary segment of unit width and length OP as shown in Fig. 3.16. If the boundary is mobile then forces F_x and F_y must act at O and P to maintain the boundary in

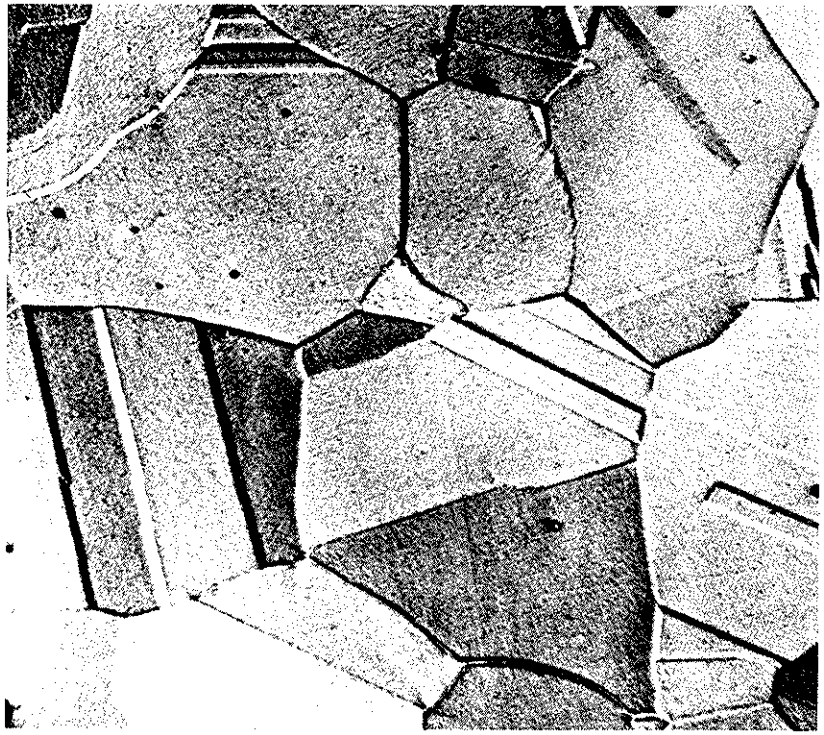

Fig. 3.15 Microstructure of an annealed crystal of austenitic stainless steel. (After P.G. Shewmon, *Transformations in Metals*, McGraw-Hill, New York, 1969.)

equilibrium. From Equation 3.3, $F_x = \gamma$. F_y can be calculated as follows: if P is moved a small distance δy while O remains stationary, the work done will be $F_y \delta y$. This must balance the increase in boundary energy caused by the change in orientation $\delta\theta$, i.e.

$$F_y \delta y = l \frac{d\gamma}{d\theta} \delta\theta$$

Since $\delta y = l\delta\theta$

$$F_y = \frac{d\gamma}{d\theta} \tag{3.12}$$

This means that if the grain-boundary energy is dependent on the orientation of the boundary (Fig. 3.16b) a force $d\gamma/d\theta$ must be applied to the ends of the boundary to prevent it rotating into a lower energy orientation. $d\gamma/d\theta$ is therefore known as a *torque term*. Since the segment OP must be supported by forces F_x and F_y the boundary exerts equal but opposite forces $-F_x$ and $-F_y$ on the ends of the segment which can be junctions with other grain boundaries.

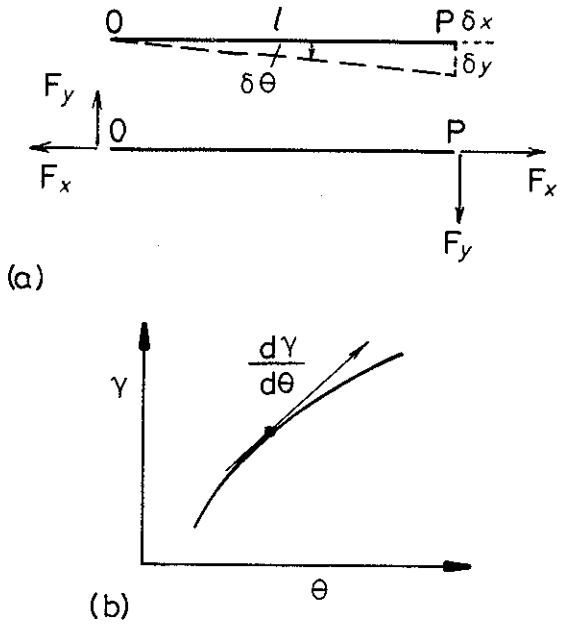

Fig. 3.16 (a) Equilibrium forces F_x and F_y supporting a length l of boundary OP. (b) The origin of F_y.

If the boundary happens to be at the orientation of a cusp in the free energy, e.g. as shown in Fig. 3.12c, there will be no torque acting on the boundary since the energy is a minimum in that orientation. However, the boundary will be able to resist a pulling force F_y of up to $(d\gamma/d\theta)_{cusp}$ without rotating.

If the boundary energy is independent of orientation the torque term is zero and the grain boundary behaves like a soap film. Under these conditions the requirement for metastable equilibrium at a junction between three grains, Fig. 3.17, is that the boundary tensions γ_1, γ_2 and γ_3 must balance. In

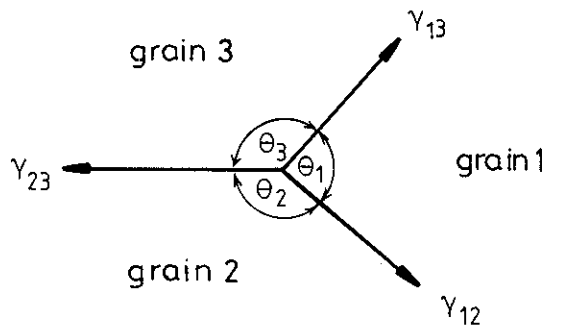

Fig. 3.17 The balance of grain boundary tensions for a grain boundary intersection in metastable equilibrium.

mathematical terms

$$\frac{\gamma_{23}}{\sin\theta_1} = \frac{\gamma_{13}}{\sin\theta_2} = \frac{\gamma_{12}}{\sin\theta_3} \tag{3.13}$$

Equation 3.13 applies to any three boundaries so that grain 1 for example could be a different phase to grains 2 and 3. Alternatively grain 1 could be a vapour phase in which case γ_{13} and γ_{12} would be the surface energies of the solid. This relationship is therefore useful for determining relative boundary energies.

One method of measuring grain-boundary energy is to anneal a specimen at a high temperature and then measure the angle at the intersection of the surface with the boundary, see Fig. 3.18. If the solid–vapour energy (γ_{sv}) is the same for both grains, balancing the interfacial tensions gives

$$2\gamma_{sv}\cos\frac{\theta}{2} = \gamma_b \tag{3.14}$$

Therefore if γ_{sv} is known γ_b can be calculated.

When using Equation 3.14 it must be remembered that the presence of any torque terms has been neglected and such an approximation may introduce large errors. To illustrate the importance of such effects let us consider the junction between coherent and incoherent twin boundary segments, Fig. 3.19. As a result of the orientation dependence of twin boundary energy, Fig. 3.12c, it is energetically favourable for twin boundaries to align themselves parallel to the twinning plane. If, however, the boundary is constrained to follow a *macroscopic plane* that is near but not exactly parallel to the twinning plane the boundary will usually develop a stepped appearance with large coherent low-energy facets and small incoherent high-energy risers as shown in Fig. 3.19. Although this configuration does not minimize the total twin boundary area it does minimize the total free energy.

It is clear that at the coherent/incoherent twin junction the incoherent twin boundary tension γ_i must be balanced by a torque term. Since the maximum value of the resisting force is $d\gamma_c/d\theta$, the condition that the configuration shown in Fig. 3.19 is stable is

$$\gamma_i \leqslant \frac{d\gamma_c}{d\theta} \tag{3.15}$$

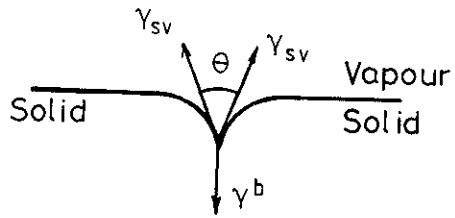

Fig. 3.18 The balance of surface and grain boundary tensions at the intersection of a grain boundary with a free surface.

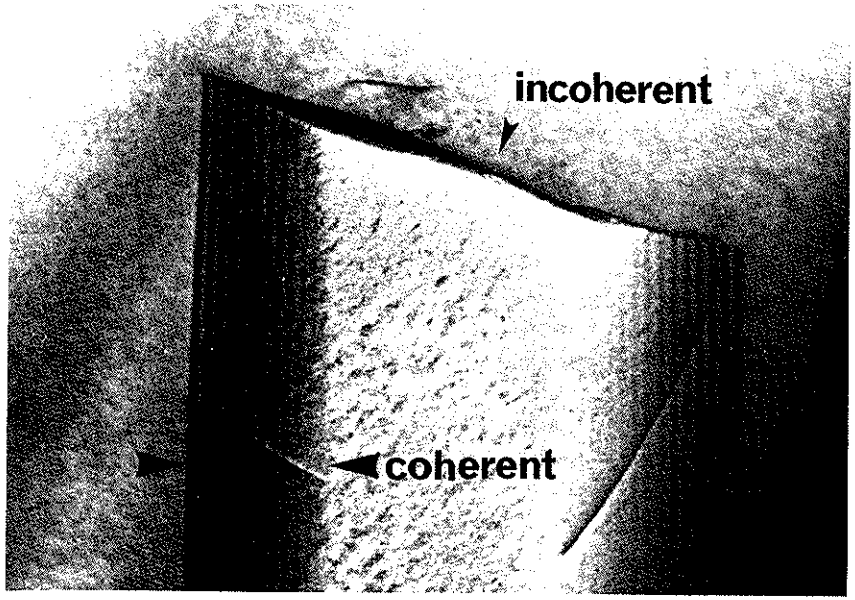

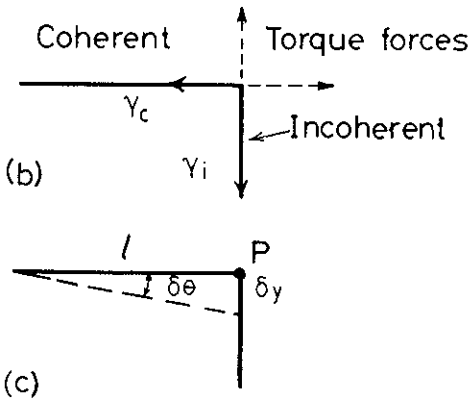

Fig. 3.19 (a) A twin boundary in a thin foil specimen as imaged in the transmission electron microscope. (After M.N. Thompson and C.W. Chen, *Philips Electron Optics Bulletin*, EM 112–1979/1 Eindhoven, 1979.) (b) and (c), the coherent and incoherent segments of the twin boundary.

Likewise the 'incoherent' facet must also be a special boundary showing rather good fit in order to provide a force resisting γ_c. That is

$$\gamma_c \leqslant \frac{d\gamma_i}{d\theta} \tag{3.16}$$

However, since γ_c is usually very small the incoherent interface need only lie in a rather shallow energy cusp.

The above can be obtained in another way from energy considerations. If (metastable) equilibrium exists at P in Fig. 3.19c, then a small displacement such as that shown should either produce no change, or an increase in the total free energy of the system, i.e.

$$dG \geqslant 0$$

Considering unit depth a small displacement δy at P will increase the total free energy by an amount

$$dG = l\frac{d\gamma_c}{d\theta}\delta\theta - \gamma_i\delta y \geqslant 0$$

Since $l\delta\theta = \delta y$ this leads to the same result as given by Equation 3.15

3.3.4 *Thermally Activated Migration of Grain Boundaries*

In the previous section it was shown that metastable equilibrium at the grain boundary junctions requires certain conditions to be satisfied for the angles at which three boundaries intersect. For simplicity, if all grain boundaries in a polycrystal are assumed to have the same grain-boundary energy independent of boundary orientation, Equation 3.13 predicts that $\theta_1 = \theta_2 = \theta_3 = 120°$. It can be similarly shown that the grain-boundary edges meeting at a corner formed by four grains will make an angle of 109° 28′. If these, or similar, angular conditions are satisfied then metastable equilibrium can be established at all grain boundary junctions. However, for a grain structure to be in complete metastable equilibrium the surface tensions must also balance over all the boundary faces between the junctions. If a boundary is curved in the shape of a cylinder, Fig. 3.20a, it is acted on by a force of magnitude γ/r towards its centre of curvature. Therefore the only way the boundary tension forces can balance in three dimensions is if the boundary is planar ($r = \infty$) or if it is curved with equal radii in opposite directions, Fig. 3.20b and c. It is

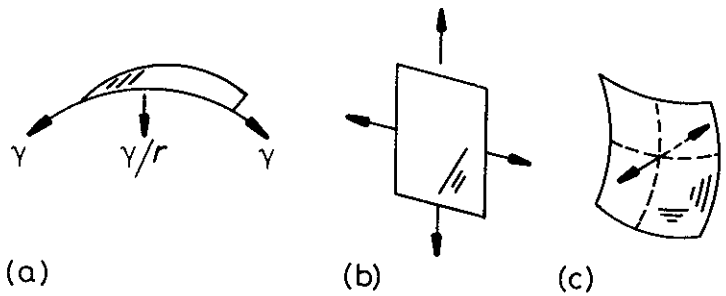

Fig. 3.20 (a) A cylindrical boundary with a radius of curvature r is acted on by a force γ/r. (b) A planar boundary with no net force. (c) A doubly curved boundary with no net force.

theoretically possible to construct a three-dimensional polycrystal in which the boundary tension forces balance at all faces and junctions, but in a random polycrystalline aggregate, typical of real metallurgical specimens, there are always boundaries with a net curvature in one direction. Consequently a random grain structure is inherently unstable and, on annealing at high temperatures, the unbalanced forces will cause the boundaries to migrate towards their centres of curvature.

The effect of different boundary curvatures in *two dimensions* is shown in Fig. 3.21. Again for simplicity it has been assumed that equilibrium at each boundary junction results in angles of 120°. Therefore if a grain has six boundaries they will be planar and the structure metastable. However, if the total number of boundaries around a grain is less than six each boundary must be concave inwards, Fig. 3.21. These grains will therefore shrink and eventually disappear during annealing. Larger grains, on the other hand, will have

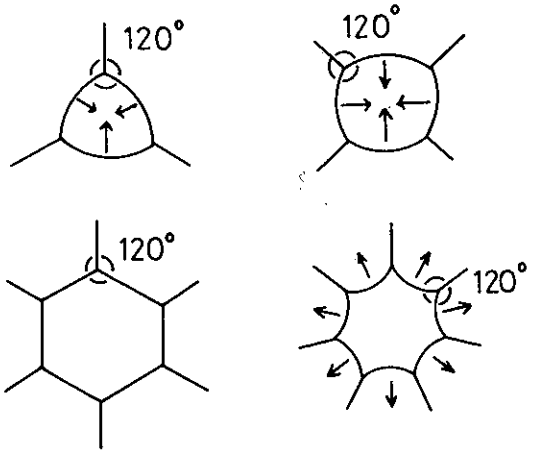

Fig. 3.21 Two-dimensional grain boundary configurations. The arrows indicate the directions boundaries will migrate during grain growth.

more than six boundaries and will grow. The overall result of such boundary migration is to reduce the number of grains, thereby increasing the mean grain size and reducing the total grain boundary energy. This phenomenon is known as *grain growth or grain coarsening*. It occurs in metals at temperatures above about 0.5 T_m where the boundaries have significant mobility. A soap froth serves as a convenient analogue to demonstrate grain growth as shown in Fig. 3.22.

In the case of the cells in a soap froth the higher pressure on the concave side of the films induces the air molecules in the smaller cells to diffuse through the film into the larger cells, so that the small cells eventually disappear. A similar effect occurs in metal grains. In this case the atoms in the shrinking grain detach themselves from the lattice on the high pressure side of the boundary and relocate themselves on a lattice site of the growing grain.

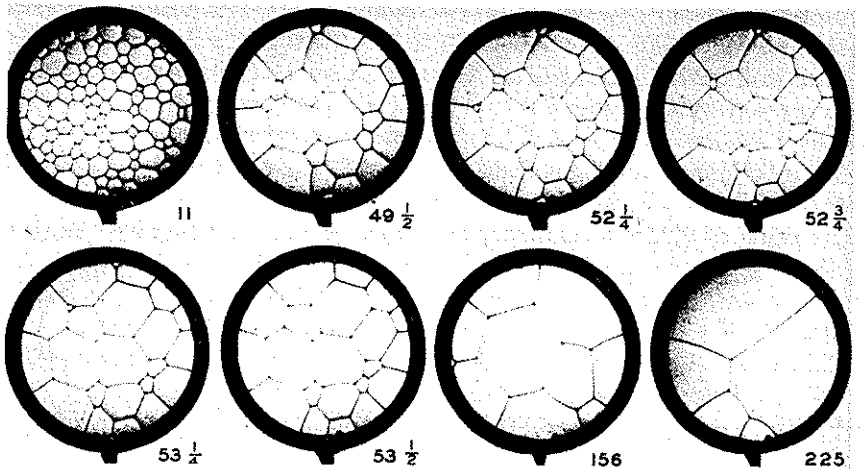

Fig. 3.22 Two-dimensional cells of a soap solution illustrating the process of grain growth. Numbers are time in minutes. (After C.S. Smith, *Metal Interfaces*, American Society for Metals, 1952, p. 81.)

For example in Fig. 3.23a if atom C jumps from grain 1 to grain 2 the boundary locally advances a small distance.

The effect of the pressure difference caused by a curved boundary is to create a difference in *free energy* (ΔG) or *chemical potential* ($\Delta\mu$) that drives the atoms across the boundary, see Fig. 3.24. In a pure metal ΔG and $\Delta\mu$ are identical and are given by Equation 1.58 as

$$\Delta G = \frac{2\gamma V_m}{r} = \Delta\mu \tag{3.17}$$

This free energy difference can be thought of as a *force* pulling the grain boundary towards the grain with the higher free energy. As shown in Fig. 3.25, if unit area of grain boundary advances a distance δx the number of moles of material that enter grain B is $\delta x \cdot 1/V_m$ and the free energy released is given by

$$\Delta G \cdot \delta x / V_m$$

This can be equated to the work done by the pulling force $F\delta x$. Thus the pulling force per unit area of boundary is given by

$$F = \frac{\Delta G}{V_m} \quad \text{N m}^{-2} \tag{3.18}$$

In other words the force on the boundary is simply the free energy difference *per unit volume* of material.

In the case of grain growth ΔG arises from the boundary curvature, but Equation 3.18 applies equally to *any* boundary whose migration causes a

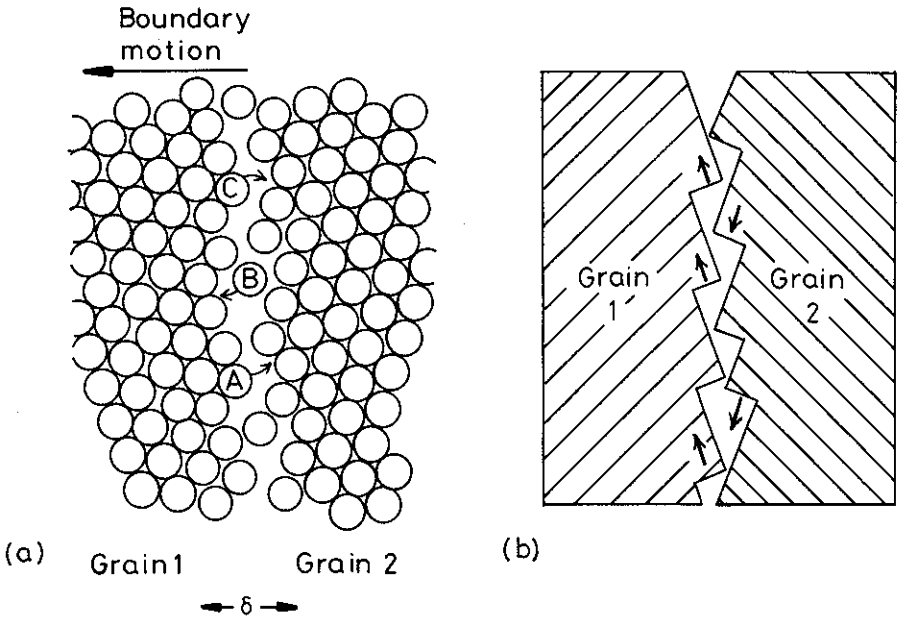

Fig. 3.23 (a) The atomic mechanism of boundary migration. The boundary migrates to the left if the jump rate from grain 1 → 2 is greater than 2 → 1. Note that the free volume within the boundary has been exaggerated for clarity. (b) Step-like structure where close-packed planes protrude into the boundary.

decrease in free energy. During recrystallization, for example, the boundaries between the new strain-free grains and the original deformed grains are acted on by a force $\Delta G/V_m$ where, in this case, ΔG is due to the difference in dislocation strain energy between the two grains. Figure 3.26 shows a dislocation-free recrystallized grain expanding into the heavily deformed surroundings. In this case the total grain-boundary area is increasing, therefore the

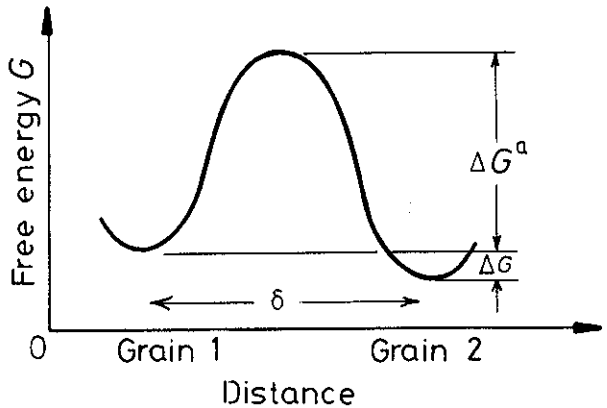

Fig. 3.24 The free energy of an atom during the process of jumping from one grain to the other.

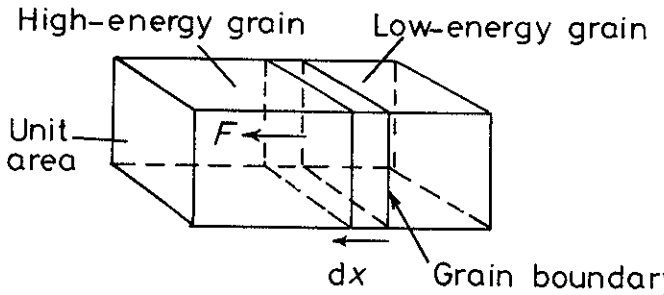

Fig. 3.25 A boundary separating grains with different free energies is subjected to a pulling force F.

Fig. 3.26 Grain boundary migration in nickel pulled 10% and annealed 10 min at 425 °C. The region behind the advancing boundary is dislocation-free. (After J. Bailey and P. Hirsch, *Proceedings of the Royal Society*, London, **A267** (1962) 11.)

driving force for recrystallization must be greater than the opposing boundary tension forces. Such forces are greatest when the new grain is smallest, and the effect is therefore important in the early stages of recrystallization.

Let us now consider the effect of the driving force on the kinetics of boundary migration. In order for an atom to be able to break away from grain 1 it must acquire, by thermal activation, an activation energy ΔG^a, Fig 3.24. If the atoms vibrate with a frequency υ_1 the number of times per second that an atom has this energy is $\upsilon_1 \exp(-\Delta G^a/RT)$. If there are on average n_1 atoms per unit area in a favourable position to make a jump there will be $n_1\upsilon_1 \exp(-\Delta G^a/RT)$ jumps $m^{-2}\,s^{-1}$ away from grain 1. It is possible that not all these atoms will find a suitable site and 'stick' to grain 2. If the probability of being accommodated in grain 2 is A_2 the effective flux of atoms from grain 1 to 2 will be

$$A_2 n_1 \upsilon_1 \exp(-\Delta G^a/RT) \quad m^{-2}\,s^{-1}$$

There will also be a similar flux in the reverse direction, but if the atoms in grain 2 have a lower free energy than the atoms in grain 1 by ΔG (mol^{-1}) the flux from 2 to 1 will be

$$A_1 n_2 \upsilon_2 \exp -(\Delta G^a + \Delta G)/RT \quad m^{-2}\,s^{-1}$$

When $\Delta G = 0$ the two grains are in equilibrium and there should therefore be no net boundary movement, i.e. the rates at which atoms cross the boundary in opposite directions must be equal. Equating the above expressions then gives

$$A_1 n_2 \upsilon_2 = A_2 n_1 \upsilon_1$$

For a high-angle grain boundary it seems reasonable to expect that there will not be great problems with accommodation so that $A_1 \simeq A_2 \simeq 1$. Assuming the above equality also holds for small non-zero driving forces, with $\Delta G > 0$ there will be a net flux from grain 1 to 2 given by

$$J_{net} = A_2 n_1 \upsilon_1 \exp\left(-\frac{\Delta G^a}{RT}\right)\left\{1 - \exp\left(-\frac{\Delta G}{RT}\right)\right\} \tag{3.19}$$

If the boundary is moving with a velocity v the above flux must also be equal to $v/(V_m/N_a)$, where (V_m/N_a) is the atomic volume. Therefore expanding $\exp(-\Delta G/RT)$ for the usual case of $\Delta G \ll RT$ gives

$$v = \frac{A_2 n_1 \upsilon_1 V_m^2}{N_a RT} \exp\left(-\frac{\Delta G^a}{RT}\right)\frac{\Delta G}{V_m} \tag{3.20}$$

In other words v should be proportional to the driving force $\Delta G/V_m$ ($N\,m^{-2}$). Equation 3.20 can be written more simply as

$$v = M \cdot \Delta G/V_m \tag{3.21}$$

where M is the mobility of the boundary, i.e. the velocity under unit driving force. Substituting for ΔG^a gives

$$M = \left\{\frac{A_2 n_1 \nu_1 V_m^2}{N_a RT} \exp\left(\frac{\Delta S^a}{R}\right)\right\} \exp\left(\frac{-\Delta H^a}{RT}\right) \tag{3.22}$$

Note how this simple model predicts an exponential increase in mobility with temperature. This result should of course be intuitively obvious since the boundary migration is a thermally activated process like diffusion. Indeed boundary migration and boundary diffusion are closely related processes. The only difference is that diffusion involves transport along the boundary whereas migration requires atomic movement across the boundary.

The model used to derive Equations 3.20 and 3.22 is particularly simple and gross assumptions are involved. In real grain boundaries it is likely that not all atoms in the boundary are equivalent and some will jump more easily than others. For example atoms may jump preferably to and from atomic steps or ledges, like atoms A, B and C in Fig. 3.23a. In fcc metals such ledges should exist where the close-packed {111} planes protrude into the boundary. Boundary migration could then be effected by the growth of the ledges in one grain combined with the shrinking of corresponding ledges in the other grain as shown in Fig. 3.23b.

From our discussion of grain-boundary structure it might be argued that the relatively open structure of a random high-angle boundary should lead to a high mobility whereas the denser packing of the special boundaries should be associated with a low mobility. Indeed, the coherent twin boundary, in which the atoms fit perfectly into both grains, has been found to be almost entirely immobile[6]. However, experiments have shown that the other special boundaries are usually more mobile than random high-angle boundaries. The reason for this is associated with the presence of impurity or alloying elements in the metal. Figure 3.27 shows data for the migration of various boundaries in zone-refined lead alloyed with different concentrations of tin. For a given driving force the velocity of the random boundaries decreases rapidly with increasing alloy content. Note that only very low concentrations of impurity are required to change the boundary mobility by orders of magnitude. The special grain boundaries on the other hand are less sensitive to impurities. It is possible that if the metal were 'perfectly' pure the random boundaries would have the higher mobility. The reason for this type of behaviour arises from differences in the interactions of alloy elements or impurities with different boundaries.

Generally the grain boundary energy of a pure metal changes on alloying. Often (though not always) it is reduced. Under these circumstances the concentration of alloying element in the boundary is higher than that in the matrix. In grain boundary segregation theory, grain boundary solute concentrations (X_b) are expressed as fractions of a monolayer. One monolayer ($X_b = 1$) means that the solute atoms in the boundary could be arranged to form a single close-packed layer of atoms. Approximately, for low mole fractions of solute in the matrix (X_0), the boundary solute concentration X_b is given by

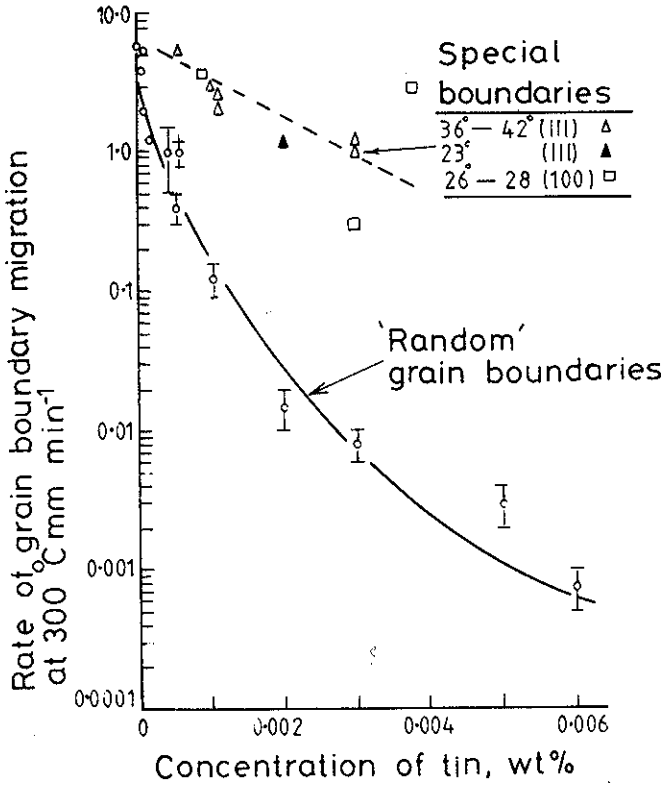

Fig. 3.27 Migration rates of special and random boundaries at 300 °C in zone-refined lead alloyed with tin under equal driving forces. (After K. Aust and J.W. Rutter, *Transactions of the Metallurgical Society of AIME*, **215** (1959) 119.)

$$X_b \simeq X_0 \exp\frac{\Delta G_b}{RT} \tag{3.23}$$

ΔG_b is the free energy released per mole when a solute atom is moved from the matrix to the boundary. ΔG_b is usually positive and roughly increases as the size misfit between the solute and matrix increases and as the solute–solute bond strength decreases.

Equation 3.23 shows how grain boundary segregation decreases as temperature increases, i.e. the solute 'evaporates' into the matrix. For sufficiently low temperatures or high values of ΔG_b, X_b increases towards unity and Equation 3.23 breaks down as X_b approaches a maximum saturation value.

The variation of boundary mobility with alloy concentration varies markedly from one element to another. It is a general rule that ΔG_b, which measures the tendency for segregation, increases as the matrix solubility decreases. This is illustrated by the experimental data in Fig. 3.28.

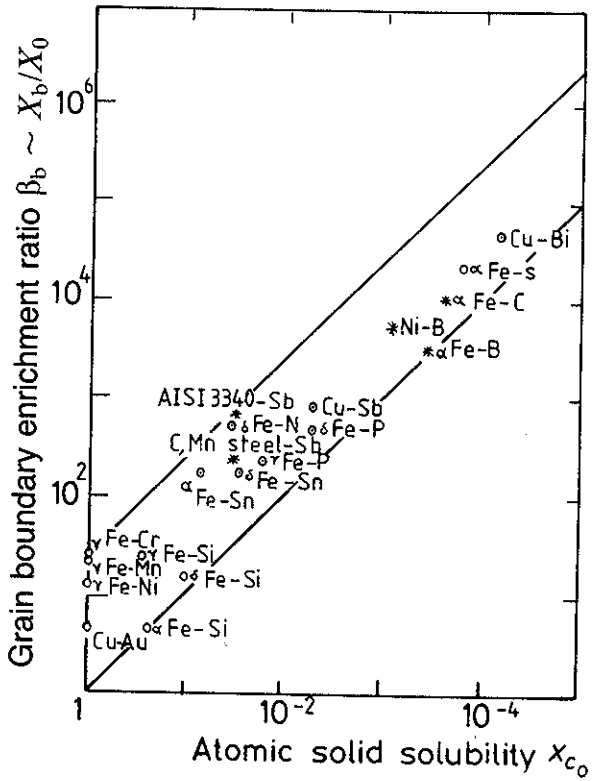

Fig. 3.28 Increasing grain boundary enrichment with decreasing solid solubility in a range of systems. (After E.D. Hondras and M.P. Seah, *International Metallurgical Reviews*, December 1977, Review 222.)

When the boundary moves the solute atoms migrate along with the boundary and exert a *drag* that reduces the boundary velocity. The magnitude of the drag will depend on the binding energy and the concentration in the boundary. The higher mobility of special boundaries can, therefore, possibly be attributed to a low solute drag on account of the relatively more close-packed structure of the special boundaries.

The variation of boundary mobility with alloy concentration varies markedly from one element to another. It is a general rule that Q_B, which measures the tendency for segregation, increases as the matrix solubility decreases. This is illustrated by the experimental data in Fig. 3.28.

It is possible that the higher mobility of special grain boundaries plays a role in the development of recrystallization textures. If a polycrystalline metal is heavily deformed, by say rolling to a 90% reduction, a deformation texture develops such that the rolled material resembles a deformed single crystal. On heating to a sufficiently high temperature new grains nucleate and begin to grow. However, not all grains will grow at the same rate: those grains which

are specially oriented with respect to the matrix should have higher mobility boundaries and should overgrow the boundaries of the randomly oriented grains. Consequently the recrystallized structure should have a special orientation with respect to the original 'single crystal'. Thus a new texture results which is called the recrystallization texture. Recrystallization is, however, incompletely understood and the above explanation of recrystallization texture may be an oversimplification. It is possible for example that the nuclei for recrystallization are themselves specially oriented with respect to the deformed matrix.

A recrystallization texture is sometimes an advantage. For example the proper texture in Fe–3wt% Si alloys makes them much better soft magnets for use in transformers. Another application is in the production of textured sheet for the deep drawing of such materials as low-carbon steel. The only way to avoid a recrystallization texture is to give an intermediate anneal before a deformation texture has been produced.

3.3.5 *The Kinetics of Grain Growth*

It was shown in the previous section that at sufficiently high temperatures the grain boundaries in a recrystallized specimen will migrate so as to reduce the total number of grains and thereby increase the mean grain diameter. In a single-phase metal the rate at which the mean grain diameter $\bar{D}$ increases with time will depend on the grain boundary mobility and the driving force for boundary migration.

If we assume that the mean radius of curvature of all the grain boundaries is proportional to the mean grain diameter $\bar{D}$ the mean driving force for grain growth will be proportional to $2\gamma/\bar{D}$ (Equation 3.17). Therefore

$$\bar{v} = \alpha M \frac{2\gamma}{\bar{D}} \simeq \frac{d\bar{D}}{dt} \tag{3.24}$$

where α is a proportionality constant of the order of unity.

Note that this equation implies that the rate of grain growth is inversely proportional to $\bar{D}$ and increases rapidly with increasing temperature due to increased boundary mobility, M. Integration of Equation 3.24 taking $\bar{D} = D_0$ when $t = 0$ gives

$$\bar{D}^2 = D_0^2 + Kt \tag{3.25}$$

where $K = 4\alpha M\gamma$.

Experimentally it is found that grain growth in single-phase metals follows a relationship of the form

$$\bar{D} = K' t^n \tag{3.26}$$

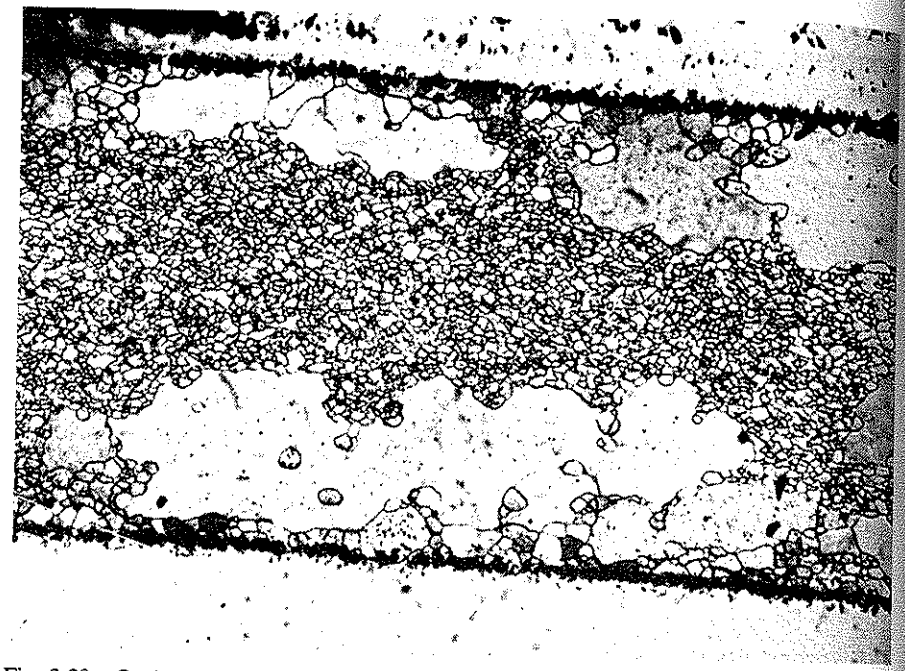

Fig. 3.29 Optical micrograph (× 130) showing abnormal grain growth in a fine-grained steel containing 0.4 wt% carbon. The matrix grains are prevented from growing by a fine dispersion of unresolved carbide particles. (After D.T. Gawne and G.T. Higgins, *Journal of the Iron and Steel Institute*, **209** (1971), 562.)

where K' is a proportionality constant which increases with temperature. This is equivalent to Equation 3.25 with $n = 0.5$ if $D \geq D_0$. However, the experimentally determined values of n are usually much less than 0.5 and only approach 0.5 in very pure metals or at very high temperatures. The reasons for this are not fully understood, but the most likely explanation is that the velocity of grain boundary migration, v, is not a linear function of the driving force, ΔG, i.e the mobility in Equation 3.21 is not a constant but varies with ΔG and therefore also with D. It has been suggested that such a variation of M could arise from solute drag effects[7].

The above type of grain growth is referred to as *normal*. Occasionally so-called *abnormal* grain growth can occur. This situation is characterized by the growth of just a few grains to very large diameters. These grains then expand consuming the surrounding grains, until the fine grains are entirely replaced by a coarse-grained array. This effect is illustrated in Fig. 3.29 and is also known as discontinuous grain growth, coarsening, or secondary recrystallization. It can occur when normal grain growth ceases due to the presence of a fine precipitate array.

The nature of normal grain growth in the presence of a second phase deserves special consideration. The moving boundaries will be attached to

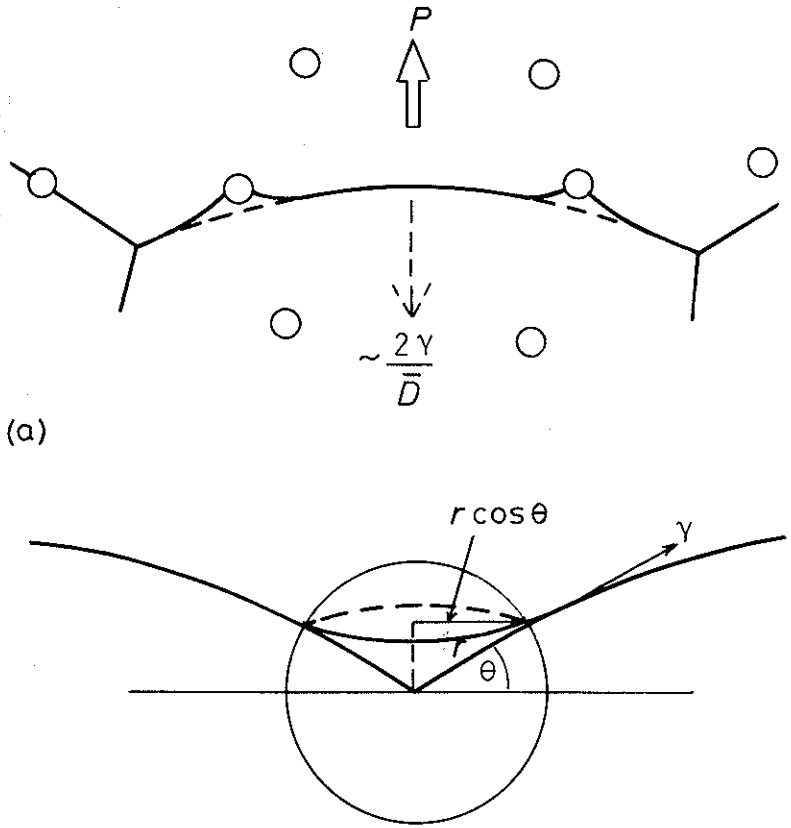

Fig. 3.30 The effect of spherical particles on grain boundary migration.

the particles as shown in Fig. 3.30a, so that the particles exert a pulling force on the boundary restricting its motion. The boundary shown in Fig. 3.30b will be attached to the particle along a length $2\pi r \cos\theta$. Therefore if the boundary intersects the particle surface at 90° the particle will feel a pull of $(2\pi r \cdot \cos\theta \cdot \gamma) \sin\theta$. This will be counterbalanced by an equal and opposite force acting on the boundary. As the boundary moves over the particle surface θ changes and the drag reaches a maximum value when $\sin\theta \cdot \cos\theta$ is a maximum, i.e. at $\theta = 45°$. The maximum force exerted by a single particle is therefore given by $\pi r\gamma$.

If there is a volume fraction f of particles all with a radius r the mean number of particles intersecting unit area of a random plane is $3f/2\pi r^2$ so that the restraining force per unit area of boundary is approximately

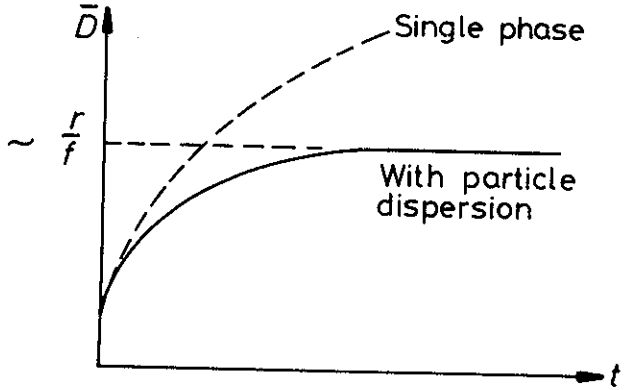

Fig. 3.31 Effect of second-phase particles on grain growth.

$$P = \frac{3f}{2\pi r^2} \cdot \pi r\gamma = \frac{3f\gamma}{2r} \tag{3.27}$$

This force will oppose the driving force for grain growth, namely $\sim 2\gamma/\bar{D}$ as shown in Fig. 3.30a. When $\bar{D}$ is small P will be relatively insignificant, but as $\bar{D}$ increases the driving force $2\gamma/\bar{D}$ decreases and when

$$\frac{2\gamma}{\bar{D}} = \frac{3f\gamma}{2r}$$

the driving force will be insufficient to overcome the drag of the particles and grain growth stagnates. A maximum grain size will be given by

$$\bar{D}_{max} = \frac{4r}{3f} \tag{3.28}$$

The effect of a particle dispersion on grain growth is illustrated in Fig. 3.31. It can be seen that the stabilization of a fine grain size during heating at high temperatures requires a large volume fraction of very small particles. Unfortunately, if the temperature is too high, the particles tend to coarsen or dissolve. When this occurs some boundaries can break away before the others and abnormal grain growth occurs, transforming the fine-grain array into a very coarse-grain structure. For example aluminium-killed steels contain aluminium nitride precipitates which stabilize the austenite grain size during heating. However, their effectiveness disappears above about 1000 °C when the aluminium nitride precipitates start to dissolve.

3.4 Interphase Interfaces in Solids

The previous section dealt in some detail with the structure and properties of boundaries between crystals of the same solid phase. In this section we will be

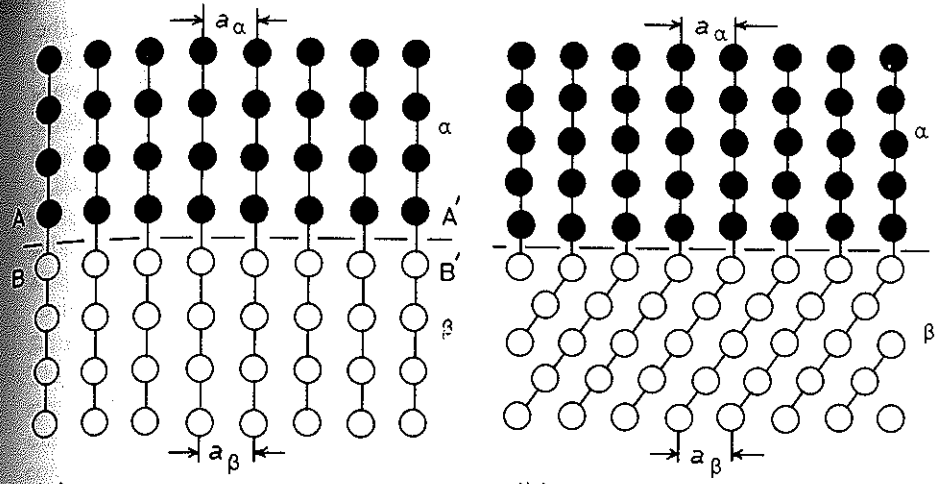

Fig. 3.32 Strain-free coherent interfaces. (a) Each crystal has a different chemical composition but the same crystal structure. (b) The two phases have different lattices.

dealing with boundaries between different solid phases, i.e. where the two adjoining crystals can have different crystal structures and/or compositions. Interphase boundaries in solids can be divided on the basis of their atomic structure into three classes: *coherent, semicoherent* and *incoherent.*

3.4.1 *Interface Coherence*

Fully Coherent Interfaces

A coherent interface arises when the two crystals match perfectly at the interface plane so that the two lattices are continuous across the interface,

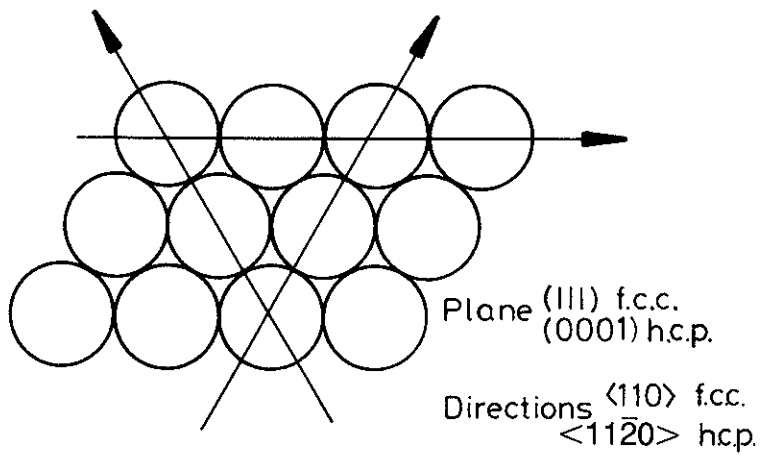

Fig. 3.33 The close-packed plane and directions in fcc and hcp structures.

Fig. 3.32. This can only be achieved if, disregarding chemical species, the *interfacial plane has the same atomic configuration in both phases*, and this requires the two crystals to be oriented relative to each other in a special way. For example such an interface is formed between the hcp silicon-rich κ phase and the fcc copper-rich α-matrix in Cu–Si alloys. The lattice parameters of these two phases are such that the $(111)_{fcc}$ plane is identical to the $(0001)_{hcp}$ plane. Both planes are hexagonally close-packed (Fig. 3.33) and in this particular case the interatomic distances are also identical. Therefore when the two crystals are joined along their close-packed planes with the close-packed directions parallel the resultant interface is completely coherent. The requirement that the close-packed planes and directions are parallel produces an *orientation relationship* between the two phases such that

$$(111)_\alpha // (0001)_\kappa$$
$$[\bar{1}10]_\alpha // [11\bar{2}0]_\kappa$$

Note that the relative orientation of two crystals can always be specified by giving two parallel planes (hkl) and two parallel directions [uvw] that lie in those planes.

Within the bulk of each phase every atom has an optimum arrangement of nearest neighbours that produces a low energy. At the interface, however, there is usually a change in composition so that each atom is partly bonded to *wrong* neighbours across the interface. This increases the energy of the interfacial atoms and leads to a chemical contribution to the interfacial energy (γ_{ch}). For a coherent interface this is the only contribution, i.e.

$$\gamma(\text{coherent}) = \gamma_{ch} \qquad (3.29)$$

In the case of the α–κ interface in Cu–Si alloys the interfacial energy has been estimated to be as low as 1 mJ m^{-2}. In general coherent interfacial energies range up to about 200 mJ m^{-2}.

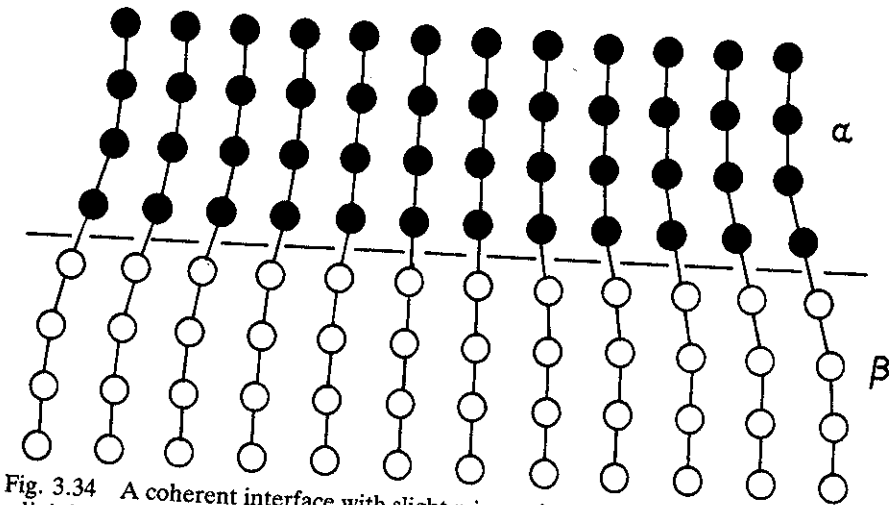

Fig. 3.34 A coherent interface with slight mismatch leads to coherency strains in the adjoining lattices.

In the case of a hcp/fcc interface there is only one plane that can form a coherent interface: no other plane is identical in both crystal lattices. If, however, the two adjoining phases have the same crystal structure and lattice parameter then, apart from differences in composition, all lattice planes are identical.

When the distance between the atoms in the interface is not identical it is still possible to maintain coherency by straining one or both of the two lattices as illustrated in Fig. 3.34. The resultant lattice distortions are known as *coherency strains*.

Semicoherent Interfaces

The strains associated with a coherent interface raise the total energy of the system, and for sufficiently large atomic misfit, or interfacial area, it becomes energetically more favourable to replace the coherent interface with a *semicoherent* interface in which the disregistry is periodically taken up by *misfit dislocations*, Fig. 3.35.

If d_α and d_β are the unstressed interplanar spacings of matching planes in the α and β phases respectively, the disregistry, or misfit between the two lattices (δ) is defined by

$$\delta = \frac{d_\beta - d_\alpha}{d_\alpha} \qquad (3.30)$$

It can be shown that in one dimension the lattice misfit can be completely accommodated without any long-range strain fields by a set of edge dislocations with a spacing D given by

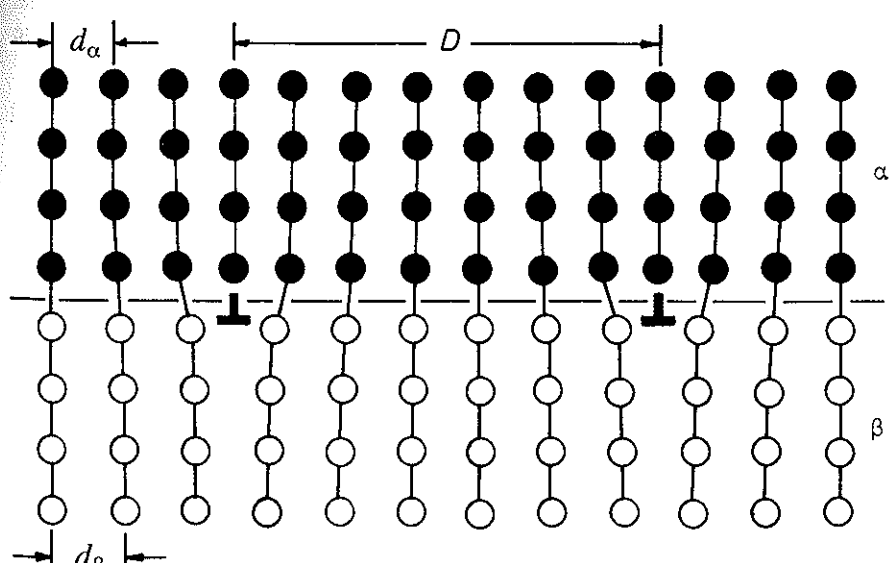

Fig. 3.35 A semicoherent interface. The misfit parallel to the interface is accommodated by a series of edge dislocations.

$$D = \frac{d_\beta}{\delta} \tag{3.31}$$

or approximately, for small δ

$$D \simeq \frac{b}{\delta} \tag{3.32}$$

where $b = (d_\alpha + d_\beta)/2$ is the Burgers vector of the dislocations. The matching in the interface is now almost perfect except around the dislocation cores where the structure is highly distorted and the lattice planes are discontinuous.

In practice misfit usually exists in two dimensions and in this case the coherency strain fields can be completely relieved if the interface contains two non-parallel sets of dislocations with spacings $D_1 = b_1/\delta_1$ and $D_2 = b_2/\delta_2$, as shown in Fig. 3.36. If, for some reason, the dislocation spacing is greater than given by Equation 3.32, the coherency strains will have been only partially relieved by the misfit dislocations and residual long-range strain fields will still be present.

The interfacial energy of a semicoherent interface can be approximately considered as the sum of two parts: (a) a chemical contribution, γ_{ch}, as for a fully coherent interface, and (b) a structural term γ_{st}, which is the extra energy due to the structural distortions caused by the misfit dislocations, i.e.

$$\gamma \text{ (semicoherent)} = \gamma_{ch} + \gamma_{st} \tag{3.33}$$

Equation 3.32 shows that as the misfit δ increases the dislocation spacing diminishes. For *small values of* δ the structural contribution to the interfacial energy is approximately proportional to the density of dislocations in the interface, i.e.

$$\gamma_{st} \propto \delta \qquad \text{(for small } \delta\text{)} \tag{3.34}$$

However γ_{st} increases less rapidly as δ becomes larger and it levels out when $\delta \simeq 0.25$ in a similar way to the variation of grain-boundary energy with θ

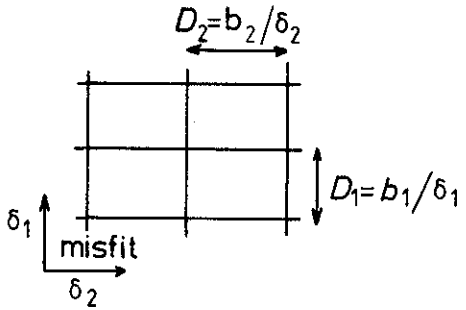

Fig. 3.36 Misfit in two directions (δ_1 and δ_2) can be accommodated by a cross-grid of edge dislocations with spacings $D_1 = b_1/\delta_1$ and $D_2 = b_2/\delta_2$.

shown in Fig. 3.9. The reason for such behaviour is that as the misfit dislocation spacing decreases the associated strain fields increasingly overlap and annul each other. The energies of semicoherent interfaces are generally in the range 200–500 mJ m^{-2}.

When $\delta > 0.25$, i.e. one dislocation every four interplanar spacings, the regions of poor fit around the dislocation cores overlap and the interface cannot be considered as coherent, i.e. it is *incoherent*.

Incoherent Interfaces

When the interfacial plane has a very different atomic configuration in the two adjoining phases there is no possibility of good matching across the interface. The pattern of atoms may either be very different in the two phases or, if it is similar, the interatomic distances may differ by more than 25%. In both cases the interface is said to be incoherent. In general, incoherent interfaces result when two randomly oriented crystals are joined across any interfacial plane as shown in Fig. 3.37. They may, however, also exist between crystals with an orientation relationship if the interface has a different structure in the two crystals.

Very little is known about the detailed atomic structure of incoherent interfaces, but they have many features in common with high-angle grain boundaries. For example they are characterized by a high energy (~500–1000 mJ m^{-2}) which is relatively insensitive to the orientation of the interfa-

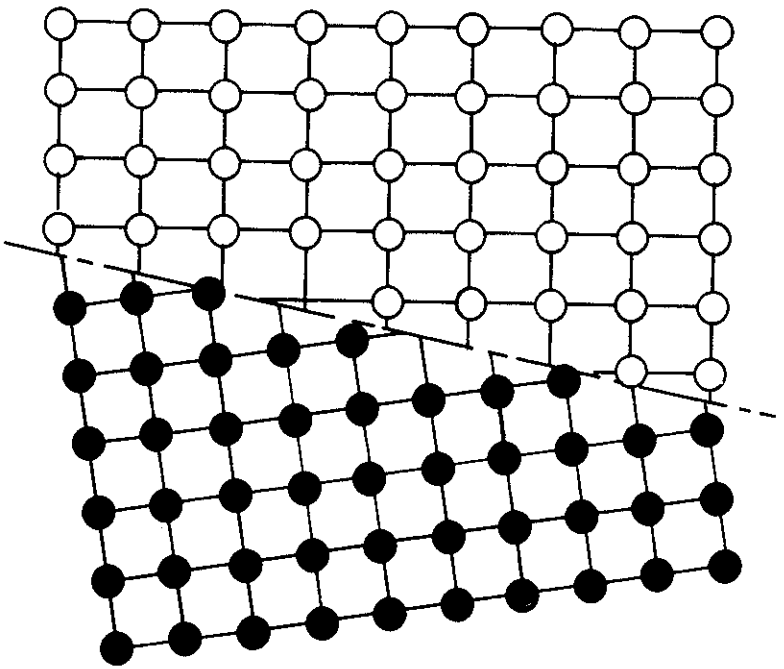

Fig. 3.37 An incoherent interface.

cial plane. They probably have a disordered atomic structure in that the interface lacks the long-range periodicity of coherent and semicoherent interfaces; although, like high-angle grain boundaries, they may have a step-like structure caused by low-index planes protruding into the interface, as in Fig. 3.23b.

Complex Semicoherent Interfaces

The semicoherent interfaces considered above have been observed at boundaries formed by low-index planes whose atom patterns and spacings are clearly almost the same. However, semicoherent interfaces, i.e. interfaces containing misfit dislocations, can also form between phases when good lattice matching is not initially obvious. For example, fcc and bcc crystals often appear with the closest-packed planes in each phase, $(111)_{fcc}$ and $(110)_{bcc}$, almost parallel to each other. Two variants of this relationship are found: the so-called Nishiyama–Wasserman (N–W) relationship:

$$(110)_{bcc}//(111)_{fcc},\ [001]_{bcc}//[\bar{1}01]_{fcc}$$

and the so-called Kurdjumov–Sachs (K–S) relationship:

$$(110)_{bcc}//(111)_{fcc},\ [1\bar{1}1]_{bcc}//[0\bar{1}1]_{fcc}$$

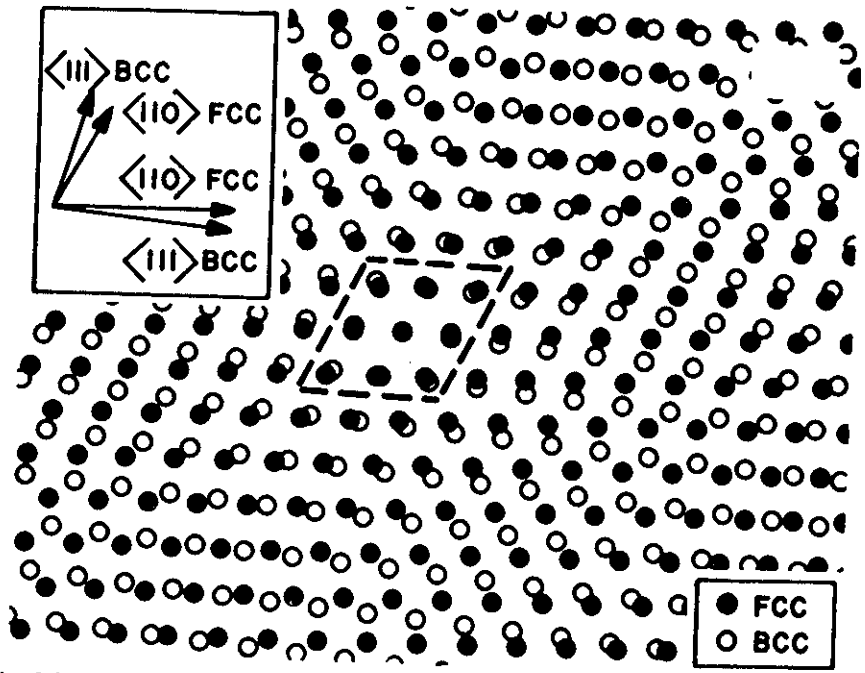

Fig. 3.38 Atomic matching across a $(111)_{fcc}/(110)_{bcc}$ interface bearing the NW orientation relationship for lattice parameters closely corresponding to the case of fcc and bcc iron (M.G. Hall *et al.*, *Surface Science*, **31** (1972) 257).

(The only difference between these two is a rotation in the closest-packed planes of 5.26°.) Figure 3.38 shows that the matching between a $\{111\}_{fcc}$ and $\{110\}_{bcc}$ plane bearing the N–W relationship is very poor. Good fit is restricted to small diamond-shaped areas that only contain ~8% of the interfacial atoms. A similar situation can be shown to exist for the K–S orientation relationship. Thus it can be seen that a coherent or semicoherent interface between the two phases is impossible for large interfaces parallel to $\{111\}_{fcc}$ and $\{110\}_{bcc}$. Such interfaces would be incoherent.

The degree of coherency can, however, be greatly increased if a macroscopically irrational interface is formed, (i.e. the indices of the interfacial plane in either crystal structure are not small integers). The detailed structure of such interfaces is, however, uncertain due to their complex nature[8,9].

3.4.2 *Second-Phase Shape: Interfacial Energy Effects*

In a two-phase microstructure one of the phases is often dispersed within the other, for example β-precipitates in an α-matrix. Consider for simplicity a system containing one β-precipitate embedded in a single α crystal, and assume for the moment that both the precipitate and matrix are strain free. Such a system will have a minimum free energy when the shape of the precipitate and its orientation relationship to the matrix are optimized to give the lowest total interfacial free energy ($\Sigma A_i\gamma_i$). Let us see how this can be achieved for different types of precipitate.

Fully Coherent Precipitates

If the precipitate (β) has the same crystal structure and a similar lattice parameter to the parent α phase the two phases can form low-energy coherent interfaces on all sides—provided the two lattices are in a parallel orientation relationship—as shown in Fig. 3.39a. This situation arises during the early stages of many precipitation hardening heat treatments, and the β phase is then termed a *fully coherent precipitate* or a *GP zone*. (GP for Guinier and Preston who first discovered their existence. This discovery was made independently by Preston in the USA and Guinier in France, both employing X-ray diffraction techniques. Their work was later confirmed by transmission electron microscopy.) Since the two crystal structures match more or less perfectly across all interfacial planes the zone can be any shape and remain fully coherent. Thus a γ-plot of the α/β interfacial energy would be largely spherical and, ignoring coherency strains, the equilibrium shape of a zone should be a sphere. Figure 3.39b shows an example of GP zones, ~10 nm in diameter, in an Al–4 atomic % Ag alloy. The zones are a silver-rich fcc region within the aluminium-rich fcc matrix. Since the atomic diameters of aluminium and silver differ by only 0.7% the coherency strains make a negligible contribution to the total free energy of the alloy. In other systems such as Al–Cu where the atomic size difference is much larger strain energy is

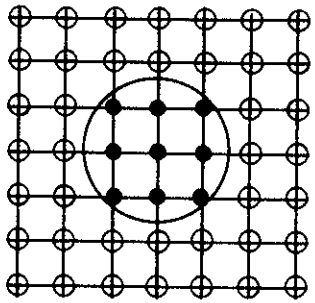

(a)

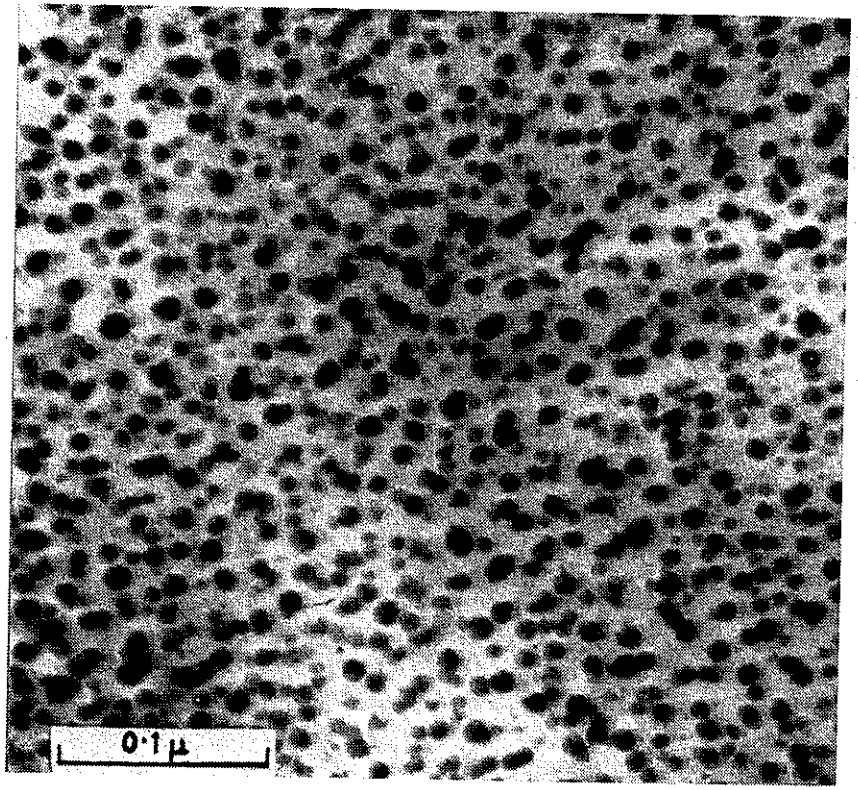

Fig. 3.39 (a) A zone with no misfit (○ Al, ● Ag, for example). (b) Electron micrograph of Ag-rich zones in an Al-4 atomic % Ag alloy (× 300 000). (After R.B. Nicholson, G. Thomas and J. Nutting, *Journal of the Institute of Metals*, **87** (1958–1959) 431.)

found to be more important than interfacial energy in determining the equilibrium shape of the zone. This point will be discussed further in Section 3.4.3.

Partially Coherent Precipitates

From an interfacial energy standpoint it is favourable for a precipitate to be surrrounded by low-energy coherent interfaces. However, when the precipitate and matrix have different crystal structures it is usually difficult to find a lattice plane that is common to both phases. Nevertheless, for certain phase combinations there may be one plane that is more or less identical in each crystal, and by choosing the correct orientation relationship it is then possible for a low-energy coherent or semicoherent interface to be formed. There are, however, usually no other planes of good matching and the precipitate must consequently also be bounded by high-energy incoherent interfaces.

A γ-plot of the interfacial energy in this case could look like that in Fig. 3.40, i.e. roughly a sphere with two deep cusps normal to the coherent interface. The Wulff theorem would then predict the equilibrium shape to be a disc with a thickness/diameter ratio of γ_c/γ_i, where γ_c and γ_i are the energies of the (semi-) coherent and incoherent interfaces. Triangular, square, or hexagonal plate shapes would be predicted if the γ plot also contained smaller cusps at symmetrically disposed positions in the plane of the plate.

The precipitate shapes observed in practice may deviate from this shape for two main reasons. Firstly the above construction only predicts the equilibrium shape if misfit strain energy effects can be ignored. Secondly the precipitate may not be able to achieve an equilibrium shape due to constraints on how it can grow. For example disc-shaped precipitates may be much wider than the equilibrium shape if the incoherent edges grow faster than the broad faces.

Plate-like precipitates occur in many systems. For example the hcp γ'-phase in aged Al–4 atomic % Ag alloys forms as plates with semicoherent

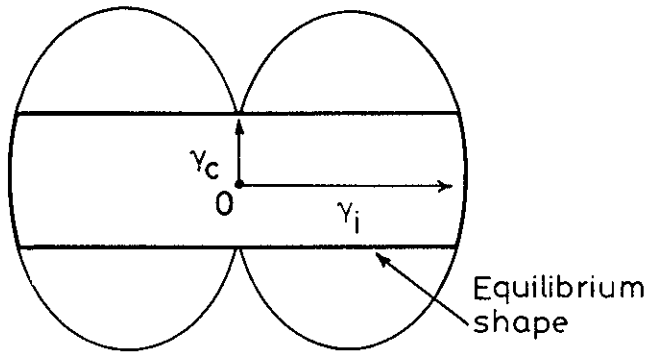

Fig. 3.40 A section through a γ-plot for a precipitate showing one coherent or semicoherent interface, together with the equilibrium shape (a disc).

broad faces parallel to the $\{111\}_\alpha$ matrix planes and with the usual hcp/fcc orientation relationship. The tetragonal θ′ phase in aged Al–4 wt% Cu alloys are also plate-shaped, but in this case the broad faces of the plate (known as the *habit plane*) are parallel to $\{100\}_\alpha$ matrix planes. Figure 3.41 shows that the $\{100\}_\alpha$ planes are almost identical to the $(001)_{\theta'}$ plane so that the orientation relationship between the θ′ and the aluminium-rich matrix (α) is

$$(001)_{\theta'}//(001)_\alpha$$
$$[100]_{\theta'}//[100]_\alpha$$

Examples of the precipitate shapes that are formed in these two systems are shown in Figs. 3.42 and 3.43. Note that as a result of the cubic symmetry of the aluminium-rich matrix there are many possible orientations for the precipitate plates within any given grain. This leads to a very characteristic crystallographic microstructure known after its discoverer as a *Widmanstätten morphology*.

Besides plate-like habits precipitates have also been observed to be lath-shaped (a plate elongated in one direction) and needle-like. For example the S phase in Al–Cu–Mg alloys forms as laths and the β′ phase in Al–Mg–Si alloys as needles[10]. In both cases the precipitates are also crystallographically related to the matrix and produce a Widmanstätten structure.

Incoherent Precipitates

When the two phases have completely different crystal structures, or when the two lattices are in a random orientation, it is unlikely that any coherent or semicoherent interfaces form and the precipitate is said to be incoherent. Since the interfacial energy should be high for all interfacial planes, the γ-plot and the equilibrium inclusion shape will be roughly spherical. It is possible

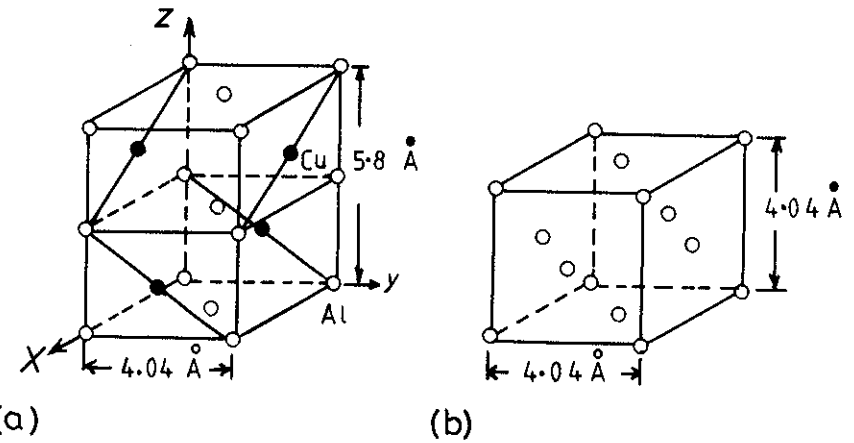

Fig. 3.41 (a) The unit cell of the θ′ precipitate in Al–Cu alloys. (b) The unit cell of the matrix. (After J.M. Silcock, T.J. Heal and H.K. Hardy, *Journal of the Institute of Metals*, **82** (1953–1954) 239.)

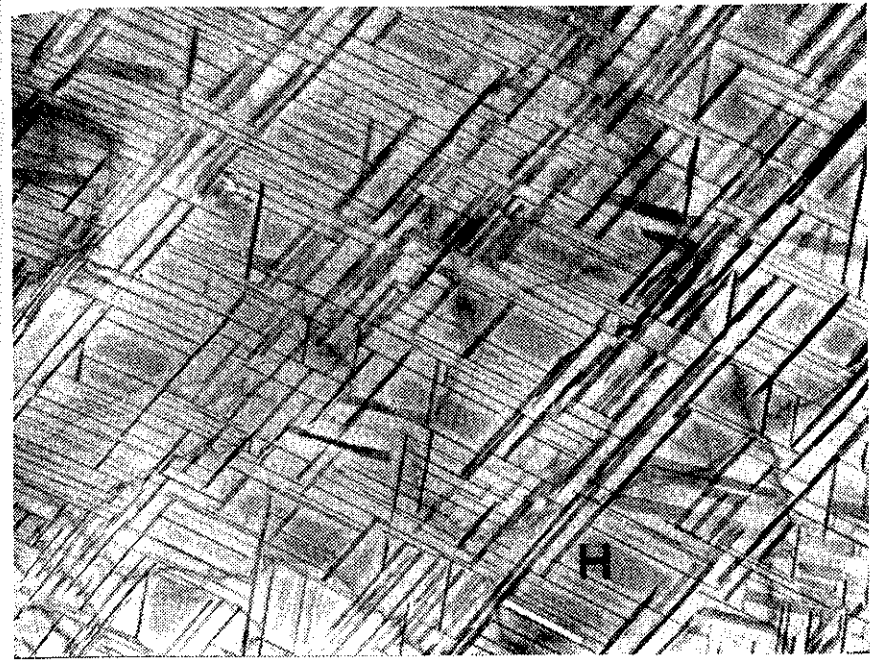

Fig. 3.42 Electron micrograph showing the Widmanstätten morphology of γ′ precipitates in an Al-4 atomic % Ag alloy. GP zones can be seen between the γ′, e.g. at H (× 7000). (R.B. Nicholson and J. Nutting, *Acta Metallurgica*, **9** (1961) 332.)

that certain crystallographic planes of the inclusion lie at cusps in the γ-plot so that polyhedral shapes are also possible. Such faceting, however, need not imply the existence of coherent or semicoherent interfaces.

The $\theta(CuAl_2)$ precipitate in Al–Cu alloys is an example of an incoherent precipitate, Fig. 3.44. It is found that there is an orientation relationship between the θ and aluminium matrix but this is probably because θ forms from the θ′ phase and does not imply that θ is semicoherent with the matrix.

Precipitates on Grain Boundaries

Rather special situations arise when a second-phase particle is located on a grain boundary as it is necessary to consider the formation of interfaces with two differently oriented grains. Three possibilities now arise (Fig. 3.45): the precipitate can have (i) incoherent interfaces with both grains, (ii) a coherent or semicoherent interface with one grain and an incoherent interface with the other, or (iii) it can have a coherent or semicoherent interface with both grains. The first two cases are commonly encountered but the third possibility is unlikely since the very restrictive crystallographic conditions imposed by coherency with one grain are unlikely to yield a favourable orientation relationship towards the other grain.

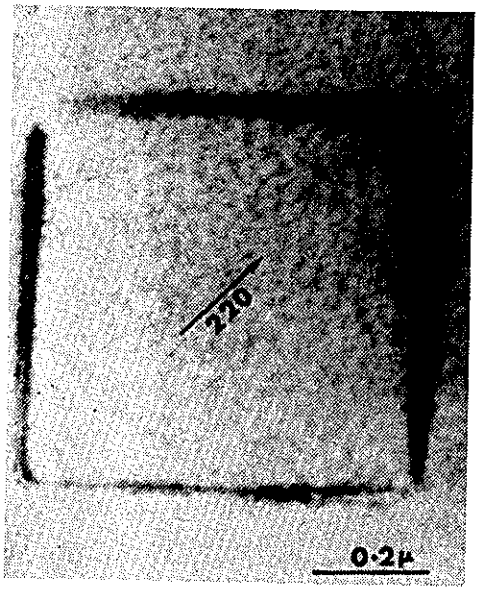

Fig. 3.43 Electron micrograph of a single coherent θ′ plate in an Al-3.9 wt% Cu alloy aged 24 h at 200 °C. (× 80 000) (R. Sankaran and C. Laird, *Acta Metallurgica* **22** (1974) 957.)

The minimization of interfacial energy in these cases also leads to planar semicoherent (or coherent) interfaces and smoothly curved incoherent interfaces as before, but now the interfacial tensions and torques must also balance at the intersection between the precipitate and the boundary. (The shape that produces the minimum free energy can in fact be obtained by superimposing the γ plots for both grains in a certain way[11].) An example of a grain-boundary precipitate is shown in Fig. 3.46.

3.4.3 *Second-Phase Shape: Misfit Strain Effects*

Fully Coherent Precipitates

It was pointed out in the previous section that the equilibrium shape of a coherent precipitate or zone can only be predicted from the γ-plot when the misfit between the precipitate and matrix is small. When misfit is present the formation of coherent interfaces raises the free energy of the system on account of the elastic strain fields that arise. If this elastic strain energy is denoted by ΔG_s the condition for equilibrium becomes

$$\Sigma A_i \gamma_i + \Delta G_s = \text{minimum} \qquad (3.35)$$

Fig. 3.44 Electron micrograph showing incoherent particles of θ in an Al–Cu alloy. (After G.A. Chadwick, *Metallography of Phase Transformations*, Butterworths, London, 1972, from C. Laird.)

The origin of the coherency strains for a misfitting precipitate is demonstrated in Fig. 3.47. If the volume of matrix encircled in Fig. 3.47a is cut out and the atoms are replaced by smaller atoms the cut-out volume will undergo a uniform negative dilatational strain to an inclusion with a smaller lattice parameter, Fig. 3.47b. In order to produce a fully coherent precipitate the matrix and inclusion must be strained by equal and opposite forces as shown in Fig. 3.47c[12].

If the lattice parameters of the unstrained precipitate and matrix are a_β and a_α respectively the *unconstrained misfit* δ is defined by

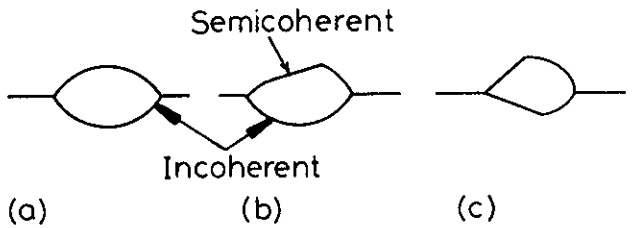

Fig. 3.45 Possible morphologies for grain boundary precipitates. Incoherent interfaces smoothly curved. Coherent or semicoherent interfaces planar.

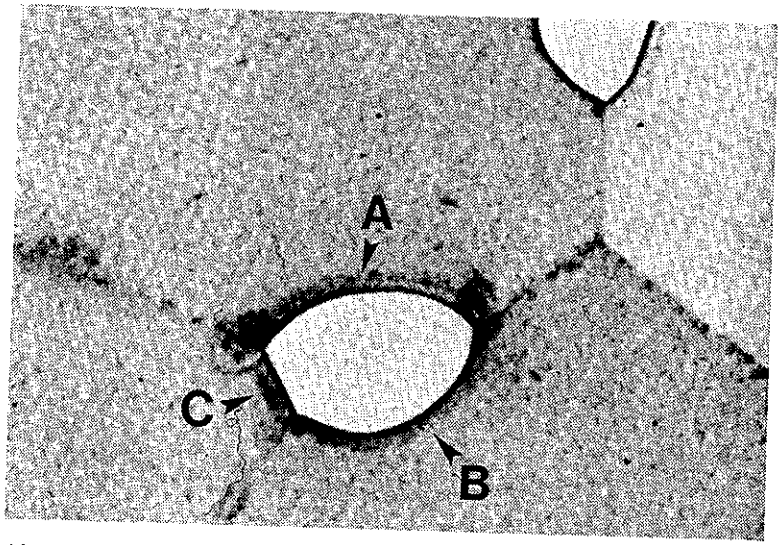

Fig. 3.46 An α precipitate at a grain boundary triple point in an α − β Cu-In alloy. Interfaces A and B are incoherent while C is semicoherent (× 310). (After G.A. Chadwick, *Metallography of Phase Transformations*, Butterworths, London, 1972.)

$$\delta = \frac{a_\beta - a_\alpha}{a_\alpha} \tag{3.36}$$

However, the stresses maintaining coherency at the interfaces distort the precipitate lattice, and in the case of a spherical inclusion the distortion is purely hydrostatic, i.e. it is uniform in all directions, giving a new lattice parameter a'_β. The *in situ* or *constrained misfit* ε is defined by

$$\varepsilon = \frac{a'_\beta - a_\alpha}{a_\alpha} \tag{3.37}$$

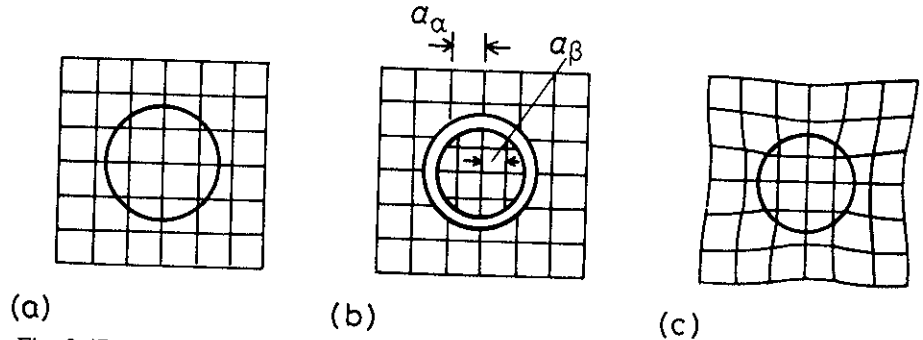

Fig. 3.47 The origin of coherency strains. The number of lattice points in the hole is conserved.

If the elastic moduli of the matrix and inclusion are equal and Poisson's ratio is 1/3, ε and δ are simply related by

$$\varepsilon = \frac{2}{3}\delta \tag{3.38}$$

In practice the inclusion has different elastic constants to the matrix, nevertheless ε still usually lies in the range $0.5\,\delta < \varepsilon < \delta$.

When the precipitate is a thin disc the *in situ* misfit is no longer equal in all directions, but instead it is large perpendicular to the disc and almost zero in the plane of the broad faces, as shown in Fig. 3.48.

In general the total elastic energy depends on the shape and elastic properties of both matrix and inclusion. However, if the matrix is elastically isotropic and both precipitate and matrix have equal elastic moduli, the total elastic strain energy ΔG_s is *independent of the shape of the precipitate*, and assuming Poissons ratio (ν) = 1/3 it is given by

$$\Delta G_s \simeq 4\mu\delta^2 \cdot V \tag{3.39}$$

where μ is the shear modulus of the matrix and V is the volume of the unconstrained hole in the matrix. Therefore coherency strains produce an elastic strain energy which is proportional to the volume of the precipitate and increases as the square of the lattice misfit (δ^2). If the precipitate and inclusion have different elastic moduli the elastic strain energy is no longer shape-independent but is a minimum for a sphere if the inclusion is hard and a disc if the inclusion is soft.

The above comments applied to isotropic matrices. In general, however, most metals are elastically anisotropic. For example, most cubic metals

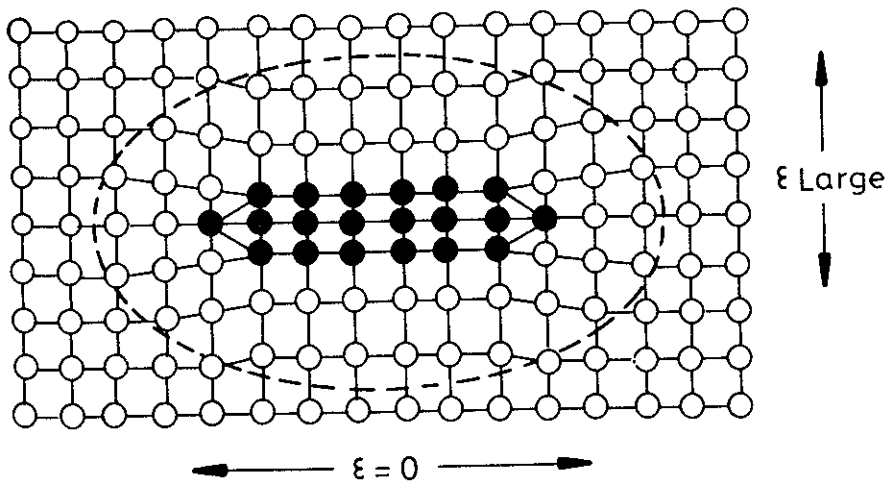

Fig. 3.48 For a coherent thin disc there is little misfit parallel to the plane of the disc. Maximum misfit is perpendicular to the disc.

(except molybdenum) are soft in ⟨100⟩ directions and hard in ⟨111⟩. The shape with a minimum strain energy under these conditions is a disc parallel to {100} since most of the misfit is then accommodated in the soft directions perpendicular to the disc.

The influence of strain energy on the equilibrium shape of coherent precipitates can be illustrated by reference to zones in various aluminium-rich precipitation hardening alloys: Al–Ag, Al–Zn and Al–Cu. In each case zones containing 50–100% solute can be produced. Assuming the zone is pure solute the misfit can be calculated directly from the atomic radii as shown below.

Atom radius (Å)	Al: 1.43	Ag: 1.44	Zn: 1.38	Cu: 1.28
Zone misfit (δ)	—	+0.7%	−3.5%	−10.5%
Zone shape	—	sphere	sphere	disc

When $\delta < 5\%$ strain energy effects are less important than interfacial energy effects and spherical zones minimize the total free energy. For $\delta \gtrsim 5\%$, as in the case of zones in Al–Cu, the small increase in interfacial energy caused by choosing a disc shape is more than compensated by the reduction in coherency strain energy.

Incoherent Inclusions

When the inclusion is incoherent with the matrix, there is no attempt at matching the two lattices and lattice sites are not conserved across the interface. Under these circumstances there are no coherency strains. Misfit strains can, however, still arise if the inclusion is the wrong size for the hole it is located in, Fig. 3.49. In this case the lattice misfit δ has no significance and it is better to consider the volume misfit Δ as defined by

$$\Delta = \frac{\Delta V}{V} \tag{3.40}$$

where V is the volume of the unconstrained hole in the matrix and $(V - \Delta V)$ the volume of the unconstrained inclusion. (For a coherent spherical inclusion

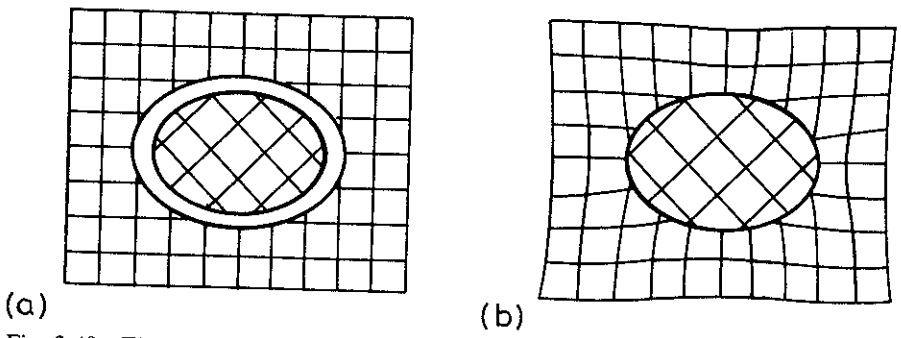

Fig. 3.49 The origin of misfit strain for an incoherent inclusion (no lattice matching).

the volume misfit and the linear lattice misfit are related by $\Delta = 3\delta$. But for a non-coherent sphere the number of lattice sites within the hole is not preserved (see Fig. 3.49) and in this case $\Delta \neq 3\delta$.) When the matrix hole and inclusion are constrained to occupy the same volume the elastic strain fields again result as shown in Fig. 3.49b. The elasticity problem in this case has been solved for spheroidal inclusions which are described by the equation

$$\frac{x^2}{a^2} + \frac{y^2}{a^2} + \frac{z^2}{c^2} = 1 \tag{3.41}$$

Nabarro[13] gives the elastic strain energy for a homogeneous incompressible inclusion in an isotropic matrix as

$$\Delta G_s = \frac{2}{3}\mu\Delta^2 \cdot V \cdot f(c/a) \tag{3.42}$$

where μ is the shear modulus of the matrix. Thus the elastic strain energy is proportional to the square of the volume misfit Δ^2. The function $f(c/a)$ is a factor that takes into account the shape effects and is shown in Fig. 3.50. Notice that, for a given volume, a sphere ($c/a = 1$) has the highest strain energy while a thin, oblate spheroid ($c/a \to 0$) has a very low strain energy, and a needle shape ($c/a = \infty$) lies between the two. If elastic anisotropy is included[14] it is found that the same general form for $f(c/a)$ is preserved and only small changes in the exact values are required. Therefore the equilibrium shape of an incoherent inclusion will be an oblate spheroid with c/a value that balances the opposing effects of interfacial energy and strain

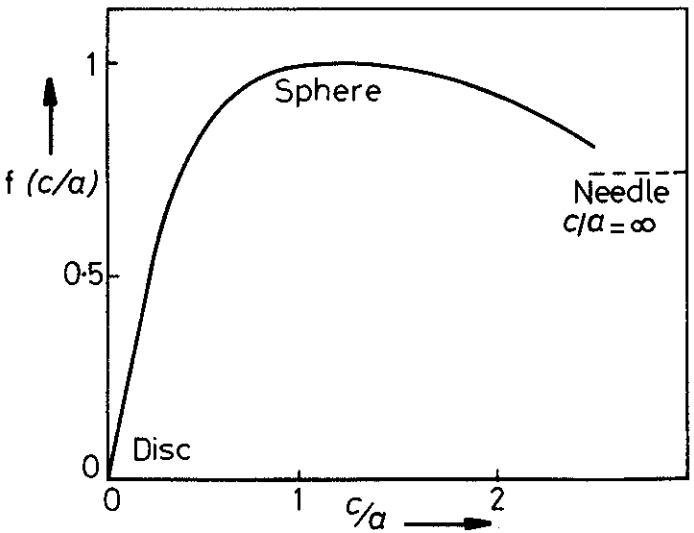

Fig. 3.50 The variation of misfit strain energy with ellipsoid shape, $f(c/a)$. (After F.R.N. Nabarro, *Proceedings of the Royal Society A*, **175** (1940) 519.)

energy. When Δ is small interfacial energy effects should dominate and the inclusion should be roughly sphercial.

Plate-Like Precipitates

Consider a plate-like precipitate with coherent broad faces and incoherent or semicoherent edges, Fig. 3.51. (The criterion for whether these interfaces are coherent or semicoherent is discussed in the following section.) Misfit across the broad faces then results in large coherency strains parallel to the plate, but no coherency strains will exist across the edges. The *in situ* misfit across the broad faces increases with increasing plate thickness which leads to greater strains in the matrix and higher shear stresses at the corners of the plates[15]. Eventually it becomes energetically favourable for the broad faces to become semicoherent. Thereafter the precipitate behaves as an incoherent inclusion with comparatively little misfit strain energy. An example of a precipitate that can be either coherent or semicoherent in this way is θ' in Al–Cu alloys (see Section 5.5.1).

3.4.4 *Coherency Loss*

Precipitates with coherent interfaces have a low interfacial energy, but in the presence of misfit, they are associated with a coherency strain energy. On the other hand, if the same precipitate has non-coherent interfaces it will have a higher interfacial energy but the coherency strain energy will be absent. Let us now consider which state produces the lowest total energy for a spherical precipitate with a misfit δ and a radius r.

The free energy of a crystal containing a fully coherent spherical precipitate has contributions from (i) the coherency strain energy given by Equation 3.39, and (ii) the chemical interfacial energy γ_{ch}. The sum of these two terms is given by

$$\Delta G(\text{coherent}) = 4\mu\delta^2 \cdot \frac{4}{3}\pi r^3 + 4\pi r^2 \cdot \gamma_{ch} \tag{3.43}$$

If the same precipitate has incoherent or semicoherent interfaces that completely relieve the unconstrained misfit there will be no misfit energy, but

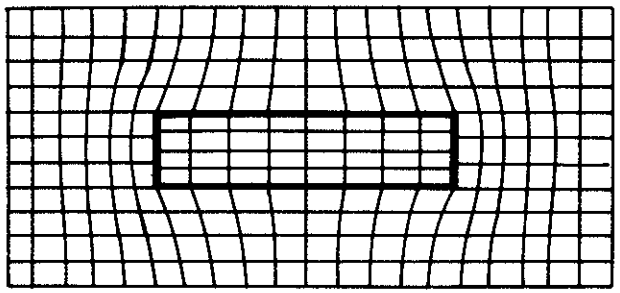

Fig. 3.51 Coherency strains caused by the coherent broad faces of θ' precipitates.

there will be an extra structural contribution to the interfacial energy γ_{st}. The total energy in this case is given by

$$\Delta G(\text{non-coherent}) = 0 + 4\pi r^2(\gamma_{ch} + \gamma_{st}) \tag{3.44}$$

For a given δ, ΔG (coherent) and ΔG (non-coherent) vary with r as shown in Fig. 3.52. When small, therefore, the coherent state gives the lowest total energy, while it is more favourable for large precipitates to be semicoherent or incoherent (depending on the magnitude of δ). At the critical radius (r_{crit}) ΔG(coherent) = ΔG(non-coherent) giving

$$r_{crit} = \frac{3\gamma_{st}}{4\mu\delta^2} \tag{3.45}$$

If we assume that δ is small, a semicoherent interface will be formed with a structural energy $\gamma_{st} \propto \delta$. In which case

$$r_{crit} \propto \frac{1}{\delta} \tag{3.46}$$

If a coherent precipitate grows, during ageing for example, it should lose coherency when it exceeds r_{crit}. However, as shown in Fig. 3.53 loss of coherency requires the introduction of dislocation loops around the precipitate and in practice this can be rather difficult to achieve. Consequently coherent precipitates are often found with sizes much larger than r_{crit}.

There are several ways in which coherency may be lost and some of them are illustrated in Fig. 3.54. The most straightforward way is for a dislocation loop to be punched out at the interface as shown in Fig. 3.54a. This requires the stresses at the interface to exceed the theoretical strength of the matrix. However, it can be shown that the punching stress p_s is independent of the precipitate size and depends only on the constrained misfit ε. If the shear modulus of the matrix is μ

$$p_s = 3\mu\varepsilon \tag{3.47}$$

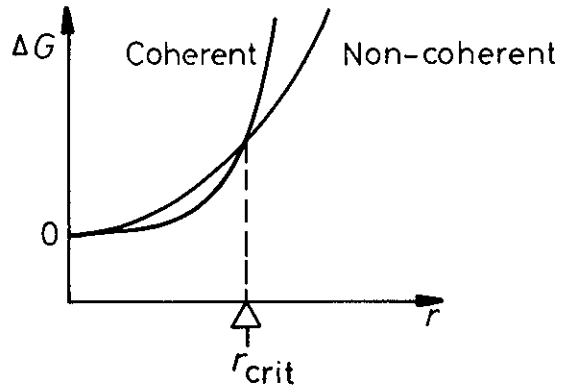

Fig. 3.52 The total energy of matrix + precipitate v. precipitate radius for spherical coherent and non-coherent (semicoherent or incoherent) precipitates.

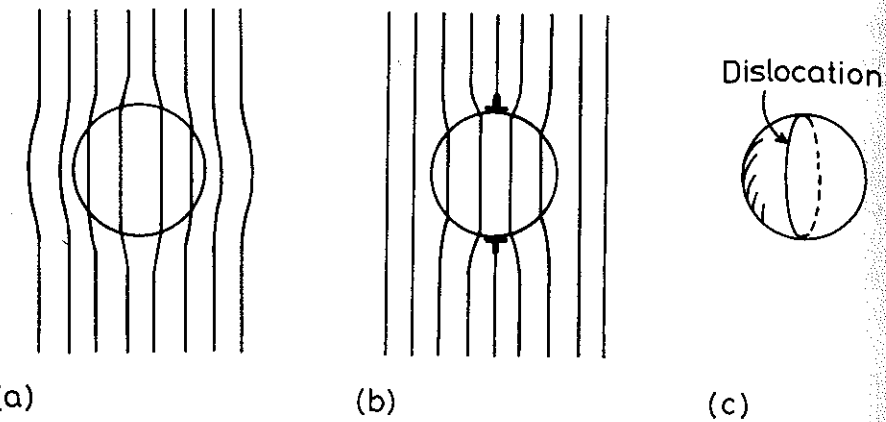

Fig. 3.53 Coherency loss for a spherical precipitate. (a) Coherent. (b) Coherency strains replaced by dislocation loop. (c) In perspective.

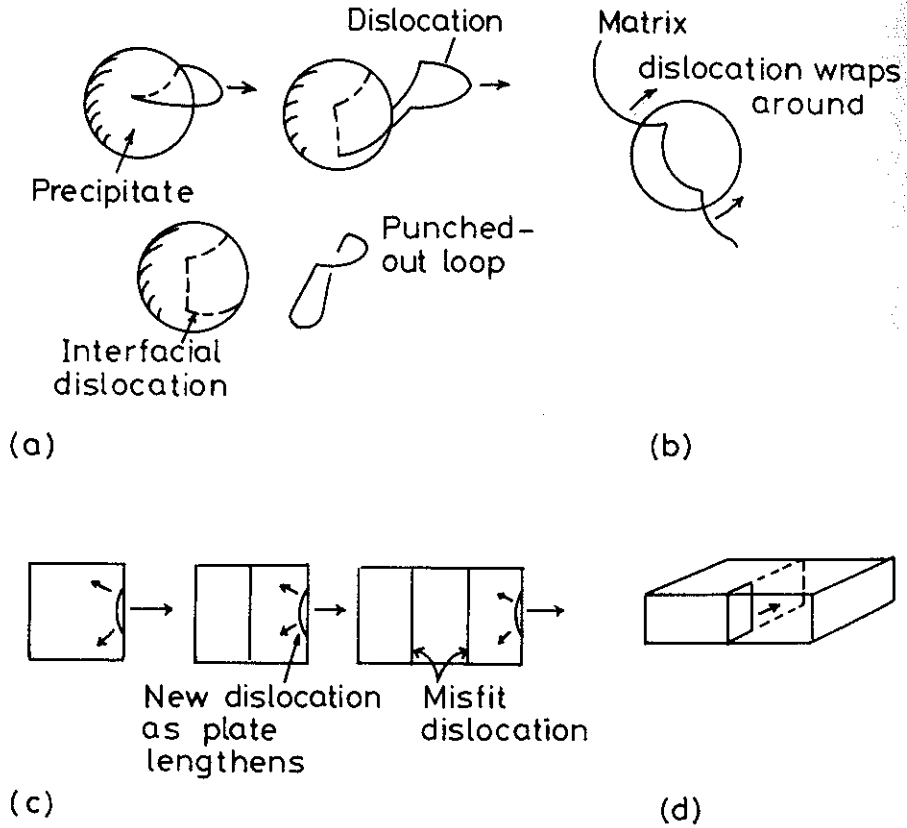

Fig. 3.54 Mechanisms for coherency loss. (a) Dislocation punching from interface. (b) Capture of matrix dislocation. (c) Nucleation at edge of plate repeated as plate lengthens. (d) Loop expansion by vacancy condensation in the precipitate.

It has been estimated that the critical value of ε that can cause the theoretical strength of the matrix to be exceeded is approximately given by

$$\varepsilon_{crit} = 0.05 \tag{3.48}$$

Consequently precipitates with a smaller value of ε cannot lose coherency by this mechanism, no matter how large.

There are several alternative mechanisms but all require the precipitate to reach a larger size than r_{crit}[16]. For example, the precipitate can attract a matrix dislocation with a suitable Burgers vector, and cause it to wrap itself around the precipitate, Fig. 3.54b. This mechanism is difficult in annealed specimens but is assisted by mechanical deformation.

In the case of plate-like precipitates the situation is different and it is now possible for the high stresses at the edges of the plates to nucleate dislocations by exceeding the theoretical strength of the matrix. The process can be repeated as the plate lengthens so as to maintain a roughly constant interdislocation spacing, Fig. 3.54c. Another mechanism that has been observed for plate-like precipitates is the nucleation of dislocation loops within the precipitate[17]. Vacancies can be attracted to coherent interfaces[18] and 'condense' to form a prismatic dislocation loop which can expand across the precipitate, as shown in Fig. 3.54d.

3.4.5 *Glissile Interfaces*

In the treatment of semicoherent interfaces that has been presented in the previous sections it has been assumed that the misfit dislocations have Burgers vectors parallel to the interfacial plane. This type of interface is referred to as epitaxial. Glide of the interfacial dislocations cannot cause the interface to advance and the interface is therefore non-glissile. It is however possible, under certain circumstances, to have glissile semicoherent interfaces which can advance by the coordinated glide of the interfacial dislocations. This is possible if the dislocations have a Burgers vector that can glide on matching planes in the adjacent lattices as illustrated in Fig. 3.55. The slip planes must be continuous across the interface, but not necessarily parallel. Any gliding dislocation shears the lattice above the slip plane relative to that below by the Burgers vector of the dislocation. In the same way the gliding of the dislocations in a glissile interface causes the receding lattice, α say, to be *sheared* into the β-structure.

As an aid to understanding the nature of glissile boundaries consider two simple cases. The first is the low-angle symmetric tilt boundary, shown in Figs. 3.7a and 3.11. In this case the Burgers vectors are all pure edge in nature and as they glide one grain is rotated into the other grain. Strictly speaking this is not an interphase interface as there is no change in crystal structure, just a rotation of the lattice. A slightly more complex example of a glissile interface between two different lattices is that which can arise between

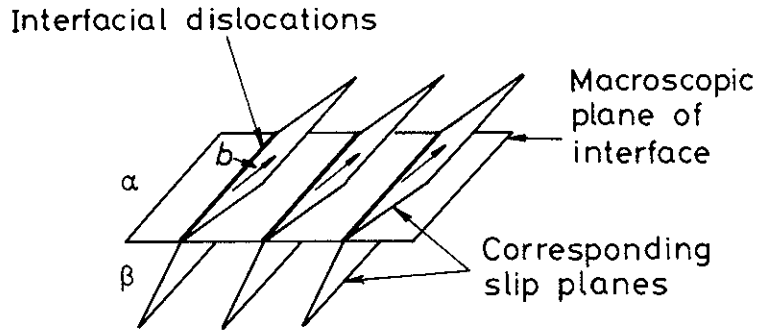

Fig. 3.55 The nature of a glissile interface.

the cubic and hexagonal close-packed lattices. To understand the structure of this interface requires a slight digression to consider the nature of *Shockley partial dislocations*.

Both fcc and hcp lattices can be formed by stacking close-packed layers of atoms one above the other. If the centres of the atoms in the first layer are denoted as A-positions, the second layer of atoms can be formed either by filling the B-positions, or C-positions as shown in Fig. 3.56. Either position produces the same atomic configuration at this stage. Let us assume therefore that the atoms in the second layer occupy B-sites. There are now two non-equivalent ways of stacking the third layer. If the third layer is placed directly above the first layer the resulting stacking sequence is ABA and the addition of further layers in the same sequence ABABABABAB . . . has hexagonal symmetry and is known as a hexagonal close-packed arrangement. The unit cell and stacking sequence of this structure are shown in Fig. 3.57. The close-packed plane can therefore be indexed as (0001) and the close-packed directions are of the type $\langle 11\bar{2}0 \rangle$.

If the atoms in the third layer are placed on the C-sites to form ABC and the same sequence is then repeated, the stacking sequence becomes ABCABCAB . . . which produces a cubic close-packed arrangement with a face-centred cubic unit cell as shown in Fig. 3.58. The close-packed atomic planes in this case become the {111} type and the close-packed directions the ⟨110⟩ type.

In terms of the fcc unit cell the distance between the B- and C-sites measured parallel to the close-packed planes corresponds to vectors of the type $\frac{a}{6}\langle 11\bar{2} \rangle$. Therefore if a dislocation with a Burgers vector $\frac{a}{6}[11\bar{2}]$ glides between two (111) layers of an fcc lattice, say layers 4 and 5 in Fig. 3.59, all layers above the glide plane (5, 6, 7 . . .) will be shifted relative to those below the glide plane by a vector $\frac{a}{6}[11\bar{2}]$. Therefore all atoms above the glide plane in B-sites are moved to C-sites, atoms in C-sites move to A-sites, and atoms in A-sites move to B-sites, as shown in Fig. 3.59. This type of dislocation with $b = \frac{a}{6}\langle 11\bar{2} \rangle$ is known as Shockley *partial* dislocation. They are called partial dislocations because vectors of the type $\frac{a}{6}\langle 11\bar{2} \rangle$ do not connect lattice

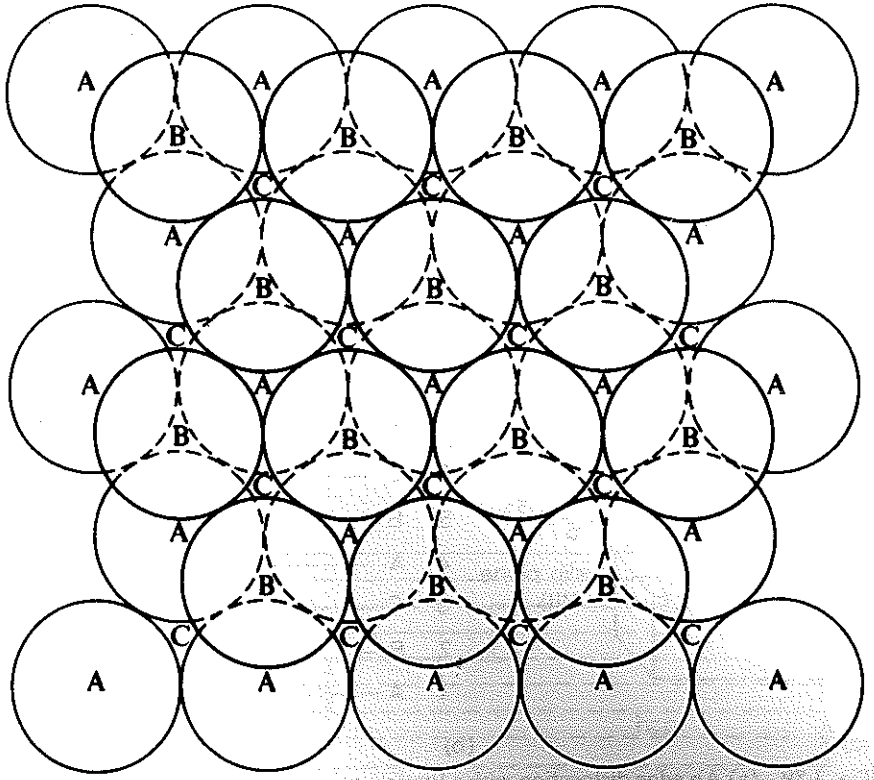

Fig. 3.56 The location of A, B and C sites in a close-packed layer of atoms. See also Figs. 3.57 and 3.58. (After J.W. Martin and R.D. Doherty, *Stability of Microstructure in Metallic Systems*, Cambridge University Press, Cambridge, 1976.)

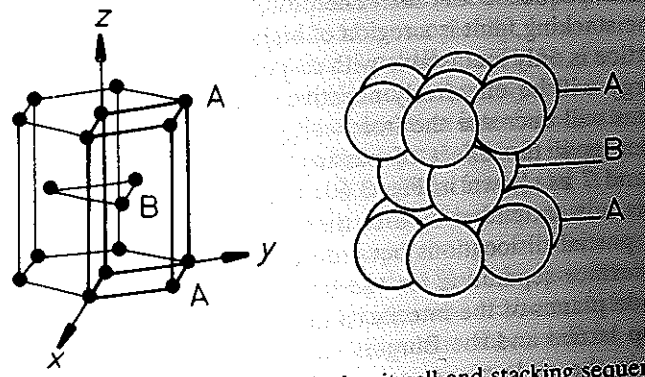

Fig. 3.57 A hexagonal close-packed unit cell and stacking sequence.

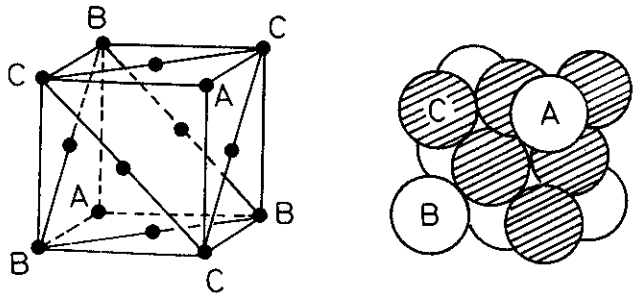

Fig. 3.58 A cubic close-packed structure showing fcc unit cell and stacking sequence.

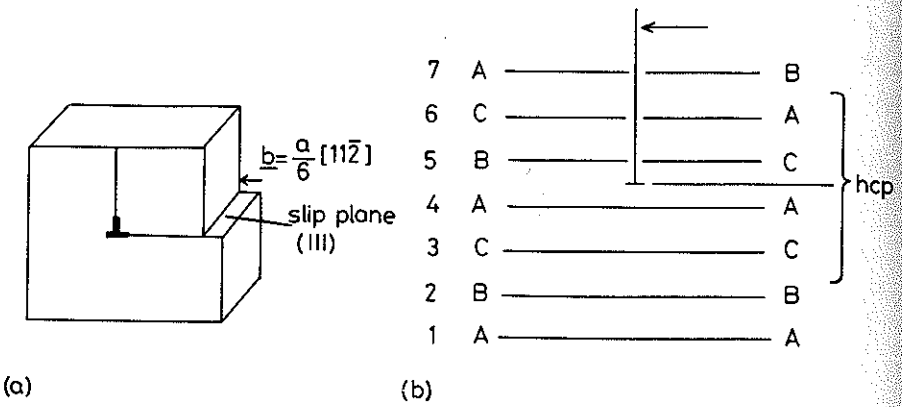

Fig. 3.59 (a) An edge dislocation with a Burgers vector $\mathbf{b} = \frac{a}{6}[11\bar{2}]$ on (111). (Shockley partial dislocation.) (b) The same dislocation locally changes the stacking sequence from fcc to hcp.

points in the fcc structure. The gliding of Shockley partial dislocations therefore disrupts the crystal lattice and causes a stacking fault over the area of glide plane swept by the dislocation. Figure 3.59 shows that the nature of this fault is such that four layers of material are converted into a hexagonal close-packed sequence CACA. Therefore in thermodynamically stable fcc lattices the stacking fault is a region of high free energy. On the other hand if the fcc lattice is only metastable with respect to the hcp structure the stacking fault energy will be effectively negative and the gliding of Shockley partial dislocations will decrease the free energy of the system.

Consider now the effect of passing another $\frac{a}{6}[11\bar{2}]$ dislocation between layers 6 and 7 as shown in Fig. 3.60. It can be seen that the region of hcp stacking is now extended by a further two layers. Therefore a sequence of Shockley partial dislocations between every other (111) plane will create a glissile interface separating fcc and hcp crystals, Fig. 3.61.

The glide planes of the interfacial dislocations are continuous from the fcc to the hcp lattice and the Burgers vectors of the dislocations, which necessarily lie in the glide plane, are at an angle to the *macroscopic* interfacial

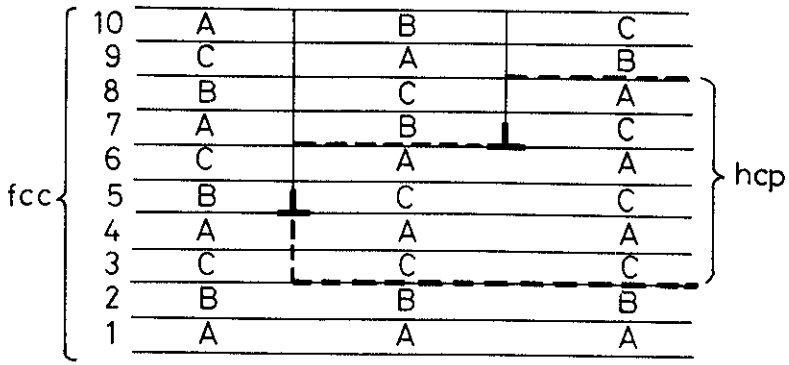

Fig. 3.60 Two Shockley partial dislocations on alternate (111) planes create six layers of hcp stacking.

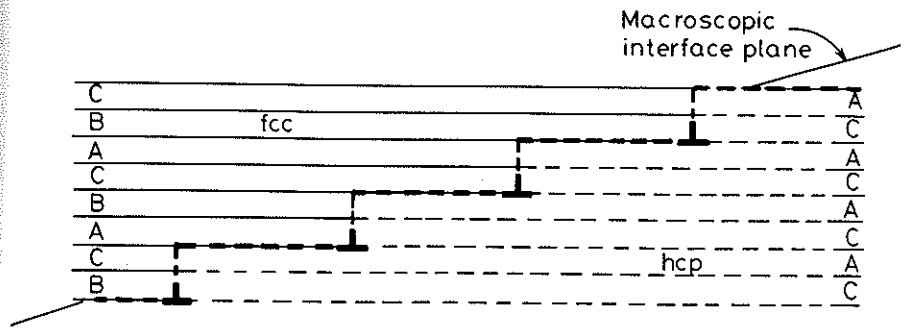

Fig. 3.61 An array of Shockley partial dislocations forming a glissile interface between fcc and hcp crystals.

plane. If the dislocation network glides into the fcc crystal it results in a transformation of fcc → hcp, whereas a hcp → fcc transformation can be brought about by the reverse motion. Macroscopically the interfacial plane lies at an angle to the (111) or (0001) planes and need not be parallel to any low-index plane, i.e. it can be *irrational*. Microscopically, however, the interface is stepped into planar coherent facets parallel to $(111)_{fcc}$ and $(0001)_{hcp}$ with a step height the thickness of two closed-packed layers.

An important characteristic of glissile dislocation interfaces is that they can produce a macroscopic *shape change* in the crystal. This is illustrated for the fcc → hcp transformation in Fig. 3.62a. If a single fcc crystal is transformed into an hcp crystal by the passage of the same Shockley partial over every (111) plane then there is a macroscopic shape change, in this case a simple shear, as shown. There are, however, two other Shockley partials which can also be used to transform fcc → hcp stacking, and if the transformation is achieved using all three partials in equal numbers there will be no overall shape change, Fig. 3.62b.

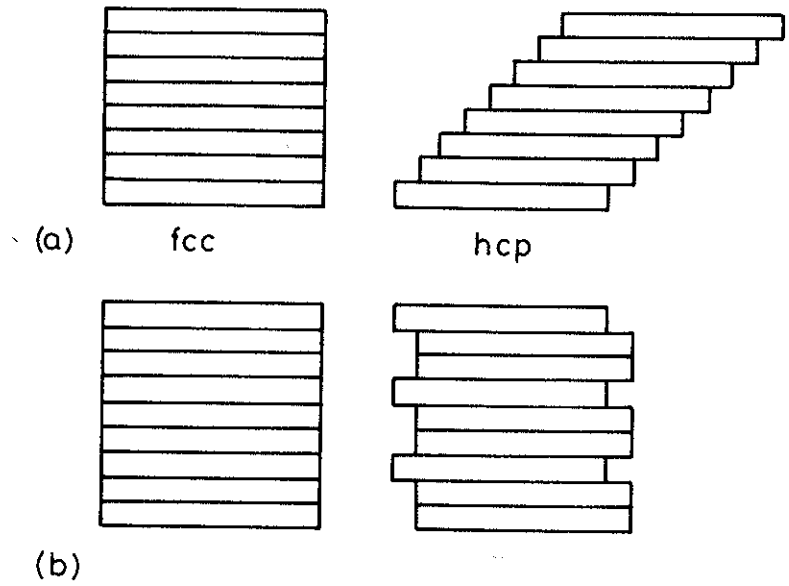

Fig. 3.62 Schematic representation of the different ways of shearing cubic close-packed planes into hexagonal close-packed (a) using only one Shockley partial, (b) using equal numbers of all three Shockley partials.

The formation of martensite in steel and other alloy systems occurs by the motion of glissile-dislocation interfaces. These transformations are characterized by a macroscopic shape change and no change in composition. Usually, however, the interface must be more complex than the fcc/hcp case discussed above, although the same principles will still apply. Martensitic transformations are dealt with further in Chapter 6.

3.4.6 *Solid/Liquid Interfaces*[19]

Many of the ideas that were discussed with regard to solid/vapour interfaces can be carried over to solid/liquid interfaces, only now the low density vapour phase is replaced by a high density liquid, and this has important consequences for the structure and energy of the interface.

There are basically two types of atomic structure for solid/liquid interfaces. One is essentially the same as the solid/vapour interfaces described in Section 3.1, i.e. an atomically flat close-packed interface, Fig. 3.63a. In this case the transition from liquid to solid occurs over a rather narrow transition zone approximately one atom layer thick. Such interfaces can also be described as smooth, faceted, or sharp. The other type is an atomically *diffuse* interface, Fig. 3.63b, in which the transition from liquid to solid occurs over several atom layers. Thus there is a gradual weakening of the interatomic bonds and an increasing disorder across the interface into the bulk liquid

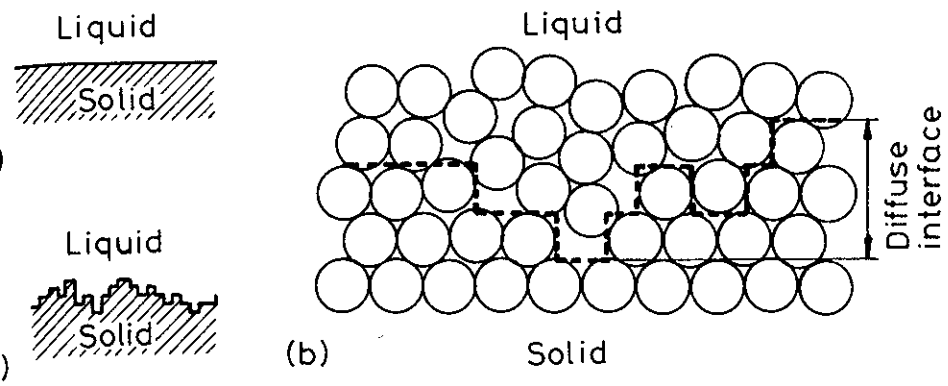

Fig. 3.63 Solid/liquid interfaces: (a) atomically smooth, (b) and (c) atomically rough, or diffuse interfaces. (After M.C. Flemings, *Solidification Processing*, McGraw-Hill, New York, 1974.)

phase; or in thermodynamic terms, enthalpy and entropy gradually change from bulk solid to bulk liquid values across the interface as shown in Fig. 3.64. When the solid and liquid are in equilibrium (at T_m) the high enthalpy of the liquid is balanced by a high entropy so that both phases have the same free energy. In the interface, however, the balance is disturbed thereby giving rise to an excess free energy, γ_{SL}.

Diffuse interfaces are also known as rough or non-faceted. The dotted line

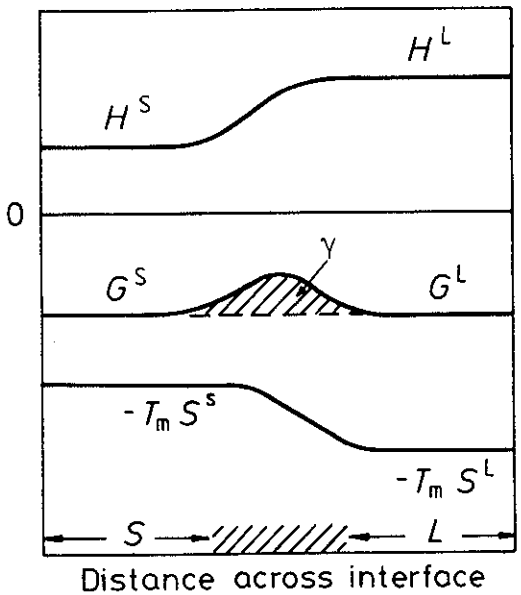

Fig. 3.64 The variation of H, $-T_mS$ and G across the solid/liquid interface at the equilibrium melting temperature T_m, showing the origin of the solid/liquid interfacial energy γ.

in Fig. 3.63b is an attempt to show the rough nature of the interface by dividing the atoms into the 'solid' and 'liquid'. If this is done the schematic representation of Fig. 3.63c can be used.

The type of structure chosen by a particular system will be that which minimizes the interfacial free energy. According to a simple theory developed by Jackson[20] the optimum atomic arrangement depends mainly on the latent heat of fusion (L_f) relative to the melting temperature (T_m). This theory predicts that there is a critical value of $L_f/T_m \simeq 4\ R$ above which the interface should be flat and below which it should be diffuse. Most metals have $L_f/T_m \simeq R$ and are therefore predicted to have rough interfaces. On the other hand some intermetallic compounds and elements such as Si, Ge, Sb as well as most non-metals have high values of L_f/T_m and generally have flat close-packed interfaces. If the model is applied to solid/vapour interfaces L_s (the heat of sublimation) should be used instead of L_f and then flat surfaces are predicted even for metals, in agreement with observations.

If the broken-bond model is applied to the calculation of the energy of a solid/liquid interface it can be argued that the atoms in the interface are roughly half bonded to the solid and half to the liquid so that the interfacial *enthalpy* should be $\sim 0.5\ L_f/N_a$ per atom. This appears to compare rather favourably with experimentally measured values of γ_{SL} which are $\sim 0.45\ L_f/N_a$ per atom for most metals. However the agreement is probably only fortuitous since entropy effects should also be taken into account, Fig. 3.64.

Some experimentally determined values of γ_{SL} are listed in Table 3.4.

Table 3.4 Experimentally Determined Solid/Liquid Interfacial Free Energies

Values selected from D. Turnbull, *Journal of Applied Physics*, Vol. **21:** 1022(1950).

Material	T_m/K	γ_{SL}/mJ m^{-2}
Sn	505.7	54.5
Pb	600.7	33.3
Al	931.7	93
Ag	1233.7	126
Au	1336	132
Cu	1356	177
Mn	1493	206
Ni	1725	255
Co	1763	234
Fe	1803	204
Pd	1828	209
Pt	2043	240

These values were determined by indirect means from homogeneous nucleation experiments (see Chapter 4) and may contain systematic errors. Comparison of Tables 3.2 and 3.3 indicates $\gamma_{SL} \simeq 0.30\gamma_b$ (for a grain boundary). More direct experiments[21] imply that $\gamma_{SL} \simeq 0.45\ \gamma_b$ ($\simeq 0.15\ \gamma_{SV}$). Another useful empirical relationship is that

$$\gamma_{SV} > \gamma_{SL} + \gamma_{LV}$$

which means that for a solid metal close to T_m it is energetically favourable for the surface to melt and replace the solid/vapour interface with solid/liquid and liquid/vapour interfaces.

It is found experimentally that the free energies of diffuse interfaces do not vary with crystallographic orientation, i.e. γ-plots are spherical[22]. Materials with atomically flat interfaces, however, show strong crystallographic effects and solidify with low-index close-packed facets, Fig. 3.65.

3.5 Interface Migration

The great majority of phase transformations in metals and alloys occur by a process known as nucleation and growth, i.e. the new phase (β) first appears

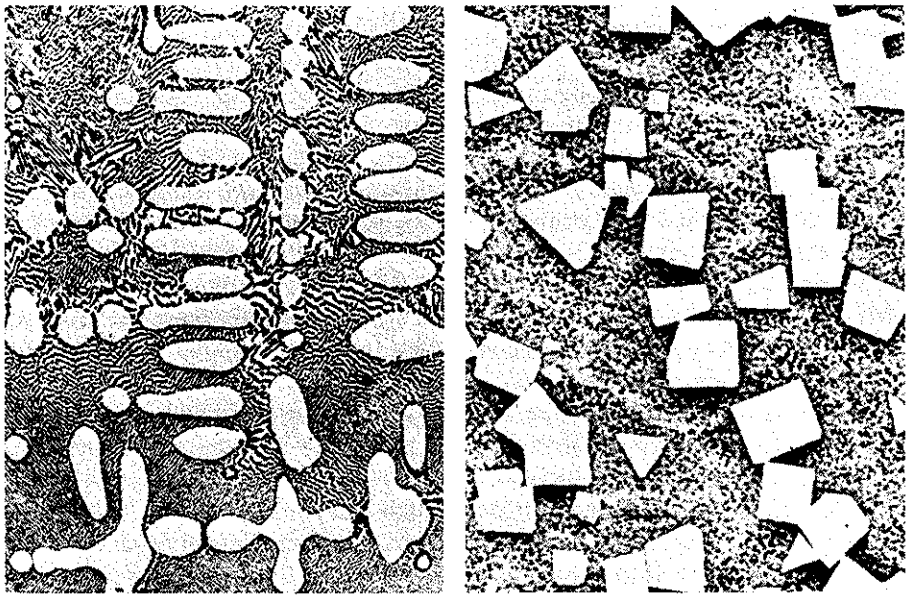

Fig. 3.65 Examples of solid–liquid interface structure in metallic systems. (a) Non-faceted dendrites of silver in a copper–silver eutectic matrix (× 330); (b) faceted cuboids of β'-SnSb compound in a matrix of Sn-rich material (× 110). (After G.A. Chadwick, *Metallography of Phase Transformations*, Butterworths, London, 1972.)

at certain sites within the metastable parent (α) phase (nucleation) and this is subsequently followed by the growth of these nuclei into the surrounding matrix. In other words, an interface is created during the nucleation stage and then migrates into the surrounding parent phase during the growth stage. This type of transformation is therefore essentially heterogeneous, i.e. at any time during the transformation the system can be divided into parent and product phases. The nucleation stage is very important and determines many features of the transformation. However, most of the transformation product is formed during the growth stage by the transfer of atoms across the moving parent/product interface.

There are basically two different types of interface: glissile and non-glissile. Glissile interfaces migrate by dislocation glide that results in the shearing of the parent lattice into the product. The motion of glissile interfaces is relatively insensitive to temperature and is therefore known as *athermal* migration. Most interfaces are non-glissile and migrate by the more or less random jumps of individual atoms across the interface in a similar way to the migration of a random high-angle grain boundary. The extra energy that the atom needs to break free of one phase and attach itself to the other is supplied by *thermal activation*. The migration of non-glissile interfaces is therefore extremely sensitive to temperature.

A convenient way of classifying nucleation and growth transformations is to divide them according to the way in which the product grows. Therefore two major groupings can be made by dividing the transformations according the whether growth involves glissile or non-glissile interfaces. Transformations produced by the migration of a glissile interface are referred to as *military transformations*. This emphasizes the analogy between the coordinated motion of atoms crossing the interface and that of soldiers moving in ranks on the parade ground. In contrast the uncoordinated transfer of atoms across a non-glissile interface results in what is known as a *civilian transformation*.

During a military transformation the nearest neighbours of any atom are essentially unchanged. Therefore the parent and product phases must have the same composition and no diffusion is involved in the transformation. Martensitic transformations belong to this group. Glissile interfaces are also involved in the formation of mechanical twins and twinning therefore has much in common with martensitic transformations.

During civilian transformations the parent and product may or may not have the same composition. If there is no change in composition, e.g. the $\alpha \rightarrow \gamma$ transformation in pure iron, the new phase will be able to grow as fast as the atoms can cross the interface. Such transformations are said to be *interface controlled*. When the parent and product phases have different compositions, growth of the new phase will require long-range diffusion. For example, the growth of the B-rich β phase into the A-rich α phase shown in Fig. 3.66 can only occur if diffusion is able to transport A away from, and B towards the advancing interface. If the interfacial reaction is fast, i.e. the transfer of atoms across the interface is an easy process, the rate at which the

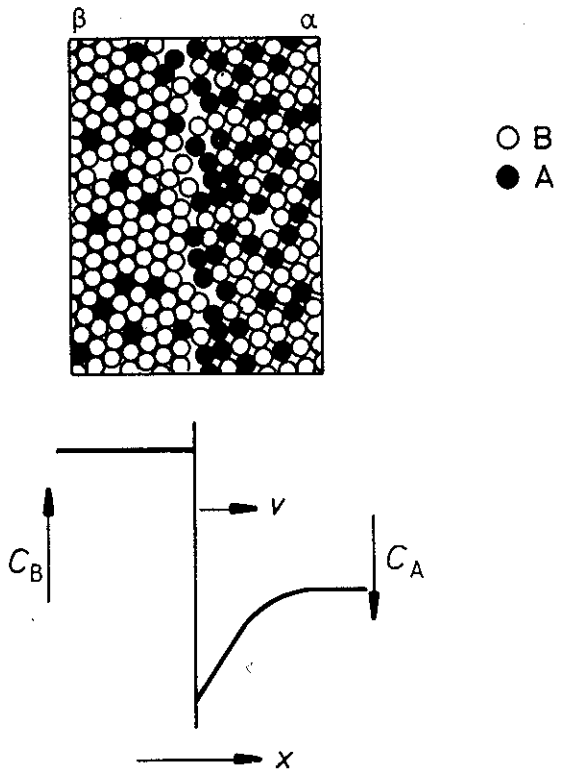

Fig. 3.66 Composition changes in a substitutional alloy caused by interface migration when the two adjoining phases have different compositions.

β phase can grow will be governed by the rate at which lattice diffusion can remove the excess atoms from ahead of the interface. This is therefore known as *diffusion-controlled* growth. However, if for some reason the interfacial reaction is slow, the growth rate will be governed by the interface kinetics. Under these circumstances growth is said to be *interface controlled* and a very small concentration gradient in the matrix is sufficient to provide the necessary flux of atoms to and from the interface. It is also possible that the interface reaction and diffusion process occur at similar rates in which case the interface is said to migrate under *mixed control*.

The above discussion of interface migration and classification of nucleation and growth transformations (also known as heterogeneous transformations) is summarized in Table 3.5, together with some examples of each class. This classification is adapted from that first proposed by Christian[23,24]. Non-glissile interfaces can be considered to include solid/liquid and solid/vapour interfaces as well as solid/solid (coherent, semicoherent and incoherent) interfaces. Therefore solidification and melting can be included in the classification of civilian transformations under diffusion control (although the concept of diffusion may sometimes need to be extended to include the diffusion of

Table 3.5 Classification of Nucleation and Growth Transformations

Type	Military	Civilian			
Effect of temperature change	Athermal	Thermally activated			
Interface type	Glissile (coherent or semicoherent)	Non-Glissile (coherent, semicoherent, incoherent, solid/liquid or solid/vapour)			
Composition of parent and product phases	Same composition	Same composition	Different compositions		
Nature of diffusion processes	No diffusion	Short-range diffusion (across interface)	Long-range diffusion (through lattice)		
Interface, diffusion or mixed control?	Interface control	Interface control	Mainly interface control	Mainly diffusion control	Mixed control
Examples	Martensite Twinning Symmetric tilt boundary	Massive Ordering Polymorphic Recrystallization Grain growth Condensation Evaporation	Precipitation Dissolution Bainite Condensation Evaporation	Precipitation Dissolution, Solidification and melting	Precipitation Dissolution Eutectoid Cellular precipitation

Adapted from J.W. Christian, 'Phase transformations in metals and alloys—an introduction', in *Phase Transformations*, Vol. 1, p. 1, Institute of Metallurgists, 1979.

heat). Condensation and evaporation at a free solid surface are also included although they will not be treated in any depth[25].

While many transformations can be easily classified into the above system, there are other transformations where difficulties arise. For example, the bainite transformation takes place by thermally activated growth, but it also produces a shape change similar to that produced by the motion of a glissile interface. At present the exact nature of such transformations is unresolved.

There is a small class of transformations, known as *homogeneous transformations* that are not covered by Table 3.5. This is because they do not occur by the creation and migration of an interface, i.e. no nucleation stage is involved. Instead the transformation occurs *homogeneously* throughout the parent phase. Spinodal decomposition and certain ordering transformations are examples of this category and they will be discussed in Chapter 5.

3.5.1 *Diffusion-Controlled and Interface-Controlled Growth*[26]

Let us now look more closely at the migration of an interface separating two phases of different composition. Consider for simplicity a β precipitate of almost pure B growing behind a planar interface into A-rich α with an initial composition X_0 as illustrated in Fig. 3.67. As the precipitate grows, the α adjacent to the interface becomes depleted of B so that the concentration of B in the α phase adjacent to the interface X_i decreases below the bulk concentration, Fig. 3.67a. Since growth of the precipitate requires a net flux of B atoms from the α to the β phase there must be a positive driving force across the interface $\Delta\mu_B^i$ as shown in Fig. 3.67b. The origin of this chemical potential difference can be seen in Fig. 3.67c. Clearly for growth to occur the interface composition must be greater than the equilibrium concentration X_e. By analogy with the migration of a high-angle grain boundary (Section 3.3.4) the net flux of B across the interface will produce an interface velocity v given by

$$v = M\Delta\mu_B^i/V_m \tag{3.49}$$

where M is the interface mobility and V_m is the molar volume of the β phase. The corresponding flux *across* the interface will be given by

$$J_B^i = -M\Delta\mu_B^i/V_m^2 \quad \text{moles of } B\ m^{-2}\ s^{-1} \tag{3.50}$$

(The negative sign indicates that the flux is in the negative direction along the x-axis.) As a result of the concentration gradient in the α phase there will also be a flux of B atoms *towards* the interface J_B^α given by

$$J_B^\alpha = -D\left(\frac{\partial C_B}{\partial x}\right)_{\text{interface}} \tag{3.51}$$

If a steady state exists at the interface these two fluxes must balance, i.e.

$$J_B^i = J_B^\alpha \tag{3.52}$$

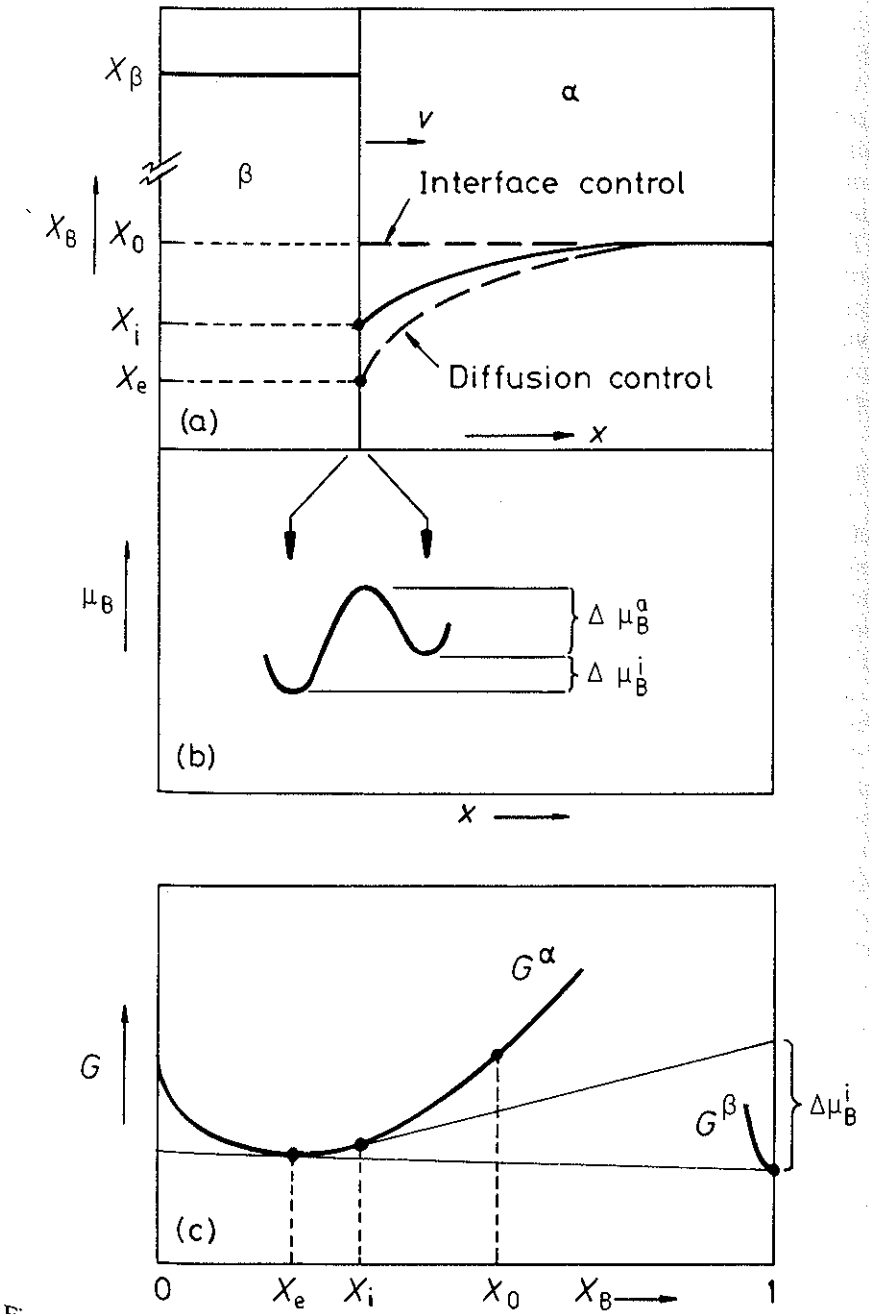

Fig. 3.67 Interface migration with long-range diffusion. (a) Composition profiles across the interface. (b) The origin of the driving force for boundary migration into the α phase. (c) A schematic molar free energy diagram showing the relationship between $\Delta\mu_B^i$, X_i and X_e. (Note that the solubility of A in the β phase is so low that the true shape of the free energy curve cannot be drawn on this scale.)

If the interface mobility is very high, e.g. an incoherent interface, $\Delta\mu_B^i$ can be very small and $X_i \simeq X_e$. Under these circumstances there is effectively *local equilibrium* at the interface. The interface will then move as fast as diffusion allows, and growth takes place under *diffusion control*. The growth rate can then be evaluated as a function of time, say, by solving the diffusion equation with the boundary conditions $X_i = X_e$ and $X_B(\infty) = X_0$. Simple examples of this problem will be given in subsequent chapters in connection with solidification and diffusive transformations in solids.

When the interface has a lower mobility a greater chemical potential difference ($\Delta\mu_B^i$) is required to drive the interface reaction and there will be a departure from local equilibrium at the interface. The value of X_i that is chosen will be that which enables Equation 3.52 to be satisfied and the interface will then be migrating under *mixed control*. In the limit of a very low mobility it is possible that $X_i \simeq X_0$ and $(\partial C/\partial x)_{\text{interface}}$ is almost zero. Under these conditions growth is said to be *interface controlled* and there is a maximum possible driving force $\Delta\mu_B^i$ across the interface.

It can easily be shown that for a dilute or ideal solution, the driving force $\Delta\mu_B^i$ is given by

$$\Delta\mu_B^i = RT\ln\frac{X_i}{X_e} \simeq \frac{RT}{X_e}(X_i - X_e) \tag{3.53}$$

provided $(X_i - X_e) << X_e$ (see exercise 3.20). Thus the rate at which the interface moves under interface control should be proportional to the deviation of the interface concentration from equilibrium $(X_i - X_e)$.

Let us now consider the question of why interface control should occur at all when the two phases have a different composition. At first sight it may appear that interface control should be very unlikely in practice. After all, the necessary long-range diffusion involves a great many atom jumps while the interface reaction essentially involves only one jump. Furthermore the activation energy for diffusion across the interface is not likely to be greater than for diffusion through the lattice—quite the contrary. On this basis, therefore, all interface reactions should be very rapid in comparison to lattice diffusion, i.e. all growth should be diffusion controlled. In many cases the above arguments are quite valid, but under certain conditions they are insufficient and may even be misleading.

Consider again the expression that was derived for the mobility of a high-angle grain boundary, Equation 3.22. A similar expression can be derived for the case of an interphase interface with $\Delta\mu_B^i$ replacing ΔG, (see exercise 3.19). It can be seen, therefore, that the above arguments neglect the effect of the accommodation factor (A), i.e. the probability that an atom crossing the boundary will be accommodated on arrival at the new phase. It is likely that incoherent interfaces and diffuse solid/liquid interfaces, as high-angle grain boundaries, will have values of A close to unity. These interfaces should therefore migrate under diffusion control. However, as will be demonstrated later, it is possible for certain types of coherent or semicoherent

interfaces, as well as smooth solid/liquid interfaces to have such low values of A that some degree of interface control is easily possible.

If two phases with different compositions, but the *same crystal structure* are separated by a coherent interface as shown in Fig. 3.32a, the interface can advance by the replacement of the α atoms in plane AA′ with β atoms by normal lattice diffusion involving vacancies. There is no need for a separate interface reaction and the migration of this type of interface is therefore diffusion controlled. This situation arises during the growth of GP zones for example. The same arguments will apply if the interface is semicoherent provided the misfit dislocations can climb by vacancy creation or annihilation.

Quite a different situation arises when the two phases forming a coherent or semicoherent interface have *different crystal structures*. Consider for example the coherent close-packed interface between fcc and hcp crystals, Fig. 3.68a. If growth of the hcp phase is to occur by individual atomic jumps (i.e. so-called continuous growth) then an atom on a C site in the fcc phase must change into a B position as shown in Fig. 3.68b. It can be seen, however, that this results in a very high energy, unstable configuration with two atoms directly above each other on B sites. In addition a loop of Shockley partial dislocation is effectively created around the atom. An atom attempting such a jump will, therefore, be unstable and be forced back to its original position. The same situation will be encountered over the coherent regions of semicoherent interfaces separating phases with different crystal structures. Solid/vapour as well as smooth solid/liquid interfaces should behave in a similar manner, though perhaps to a lesser extent. If a single atom attaches itself to a flat close-packed interface it will raise the interfacial free energy and will therefore tend to detach itself again. It can thus be seen that continuous growth at the above type of interfaces will be very difficult, i.e. very low accommodation factors and low mobility are expected.

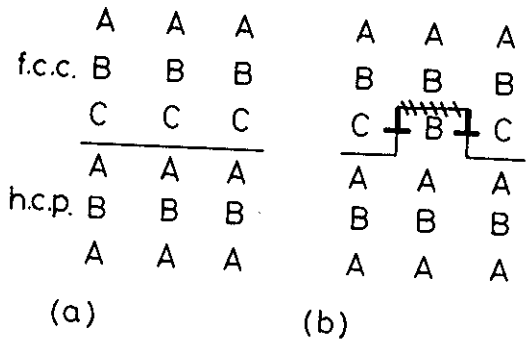

Fig. 3.68 Problems associated with the continuous growth of coherent interfaces between phases with different crystal structures. (After J.W. Martin and R.D. Doherty, *Stability of Microstructure in Metallic Systems*, Cambridge University Press, Cambridge, 1976.)

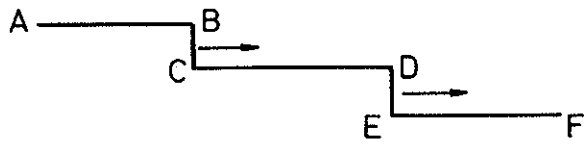

Fig. 3.69 The ledge mechanism.

A way of avoiding the difficulties of continuous growth encountered in the above cases is provided by the 'ledge' mechanism shown in Fig. 3.69. If the interface contains a series of ledges BC, DE normal to the facets AB, CD, EF, atoms will be able to transfer more easily across the ledges than the immobile facets and interface migration is therefore effected by the transverse migration of the ledges as shown.

Growth ledges have in fact been seen with the aid of the electron microscope on the surfaces of growing precipitates. For example Fig. 3.70 shows an electron micrograph and a schematic drawing of the growth ledges on an Mg_2Si plate in an Al–Mg–Si alloy[27]. Note that growth ledges are usually hundreds of atom layers high.

When existing ledges have grown across the interface there is a problem of generating new ones. In Fig. 3.70 the source of new ledges is thought to be heterogeneous nucleation at the point of contact with another precipitate. The same problem will not be encountered if the precipitate is dissolving, however, since the edges of the plate will provide a continual source of ledges[28]. It is thought that once nucleated, the rate at which ledges migrate across the planar facets should be diffusion controlled, i.e. controlled by how fast diffusion can occur to and from the ledges. However, the problem of nucleating new ledges may often lead to a degree of interface control on the overall rate at which the coherent or semicoherent interface can advance perpendicular to itself.

Growth ledges are by no means restricted to solid/solid systems. The first evidence for the existence of growth ledges came from studies of solid/vapour interfaces. They are also found on faceted solid/liquid interfaces.

The mechanism of interface migration can have important effects on the shape of second-phase inclusions. It was shown in Section 3.4.2 that in the absence of strain energy effects the *equilibrium shape* of a precipitate should be determined by the relative energies of the bounding interfaces. For example, a partially coherent precipitate should be disc or plate shaped with an aspect ratio of γ_i/γ_c where γ_i is the energy of the incoherent edges and γ_c is the energy of the coherent or semicoherent broad faces. However, the precipitate shape observed in practice may be prevented from achieving this equilibrium shape by the relative rates at which the coherent and incoherent interfaces can migrate. For example if there are problems of ledge nucleation the easier growth of the incoherent plate edges may lead to a larger aspect ratio than the equilibrium.

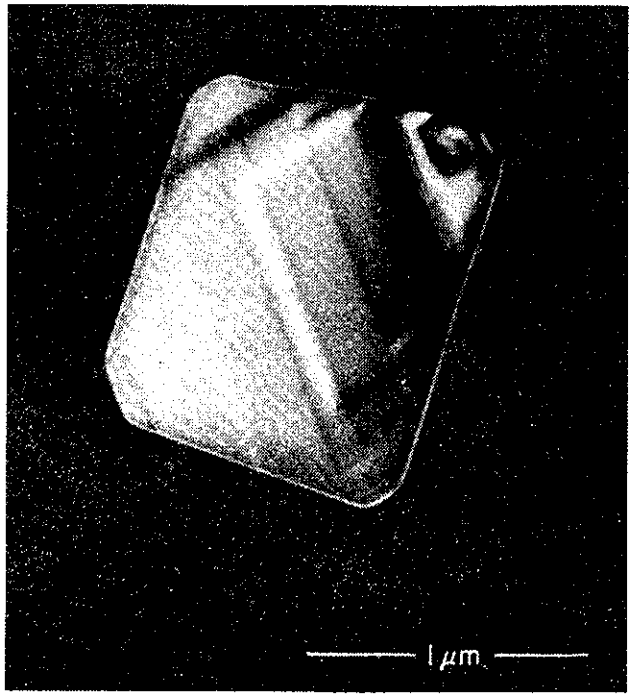

Fig. 3.70 (a) Growth ledges at an Mg_2Si plate in Al–1.5 wt% Mg_2Si, solution treated and aged 2 h at 350 °C. Dark field micrograph. (b) Schematic diagram of (a) showing ledges on Mg_2Si plate. (After G.C. Weatherly, *Acta Metallurgica*, **19** (1971) 181.)

References

1. This subject is covered in detail in J.W. Martin and R.D. Doherty *Stability of Microstructure in Metallic Systems*, Cambridge University Press, 1976, and in M. McLean 'Miscrostructural instabilities in metallurgical systems—a review' *Metal Science*, March 1978, p. 113.
2. Methods are described in J.M. Blakely, *Introduction to the properties of crystal surfaces*, Pergamon, Oxford, 1973, p. 53.

3. For a more detailed discussion, see J.W. Christian, *The Theory of Transformations in Metals and Alloys*, Second Edition, Part I, Pergamon, Oxford, 1975, p. 153.
4. R.S. Nelson, D.J. Mazey and R.S. Barnes, *Philosophical Magazine*, **11**:91 (1965).
5. Sundquist, *Acta Metallurgica*, **12**:67 (1964).
6. C.J. Simpson, K.T. Aust and W.C. Winegard, *Scripta Met.*, **3**:171 (1969).
7. See for example J.W. Martin and R.W. Doherty, *Stability of Microstructure in Metallic Systems*, Cambridge University Press, 1976, p. 221.
8. J.W. Christian, *Metallurgical Transactions*, **21A**: 799 (1990).
9. J.W. Christian, *Materials Science and Engineering*, **A127**: 215 (1990).
10. G.C. Weatherly and R.B. Nicholson, *Phil. Mag.* **17**:801 (1968).
11. The interested reader is referred to M.I. Aaronson and J.K. Lee, 'Lectures on the theory of phase transformations', H.I. Aaronson (Ed.), Met. Soc. AIME, New York, 1975.
12. A quite general method for calculating the stress and strain fields in and around misfitting inclusions has been elucidated by J.D. Eshelby in *Proc. Roy. Soc., London*, **A241** (1957) p. 376, and in *Progress in Solid Mechanics*, **II**, Chapter III (1961).
13. F.R.N. Nabarro, *Proc. Roy. Soc.* **A175**: 519 (1940).
14. Jong K. Lee and William C. Johnson, *Acta Metallurgica* **26**:541–545 (1978).
15. R. Sankaran and C. Laird, *J. Mech. Phys. Solids*, **24**:251–262 (1976) and *Phil. Mag.*, **29**:179 (1974).
16. L.M. Brown and G.R. Woolhouse, *Phil. Mag.*, **21**:329 (1970).
17. R. Sankaran and C. Laird, *Phil. Mag.*, **29**:179 (1974).
18. K.E. Easterling and T. Johannesson, *Phil. Mag.*, **24**:981 (1971).
19. A detailed treatment of solid/liquid interfaces can be found in D.P. Woodruff *The Solid-Liquid Interface*, Cambridge University Press, 1973.
20. K.A. Jackson, *Liquid Metals and Solidification*, ASM, Cleveland, Ohio (1958), p. 174.
21. W.A. Miller and G.A Chadwick, *Acta Metallurgica*, **15**:607 (1967).
22. W.A. Miller and G.A. Chadwick, Proc. *Roy. Soc.* **A312**:251 (1969).
23. J.W. Christian, *The Theory of Transformations in Metals and Alloys*, Edition 2, Part 1, Pergamon, 1975, p. 9.
24. J.W. Christian, 'Phase transformations in metals and alloys—an introduction', in *Phase Transformations*, **1**, p. 1, Institute of Metallurgists, 1979.
25. The interested reader is referred to E. Rutner *et al.* (Eds.), *Condensation and Evaporation of Solids*, Gordon and Breach, New York, 1964.
26. For an advanced discussion of this subject see M. Hillert, 'Diffusion and interface control of reactions in alloys', *Met. Trans. A.*, **6A**:5 (1975).
27. G.C. Weatherly, *Acta Metallurgica*, **19**:181 (1971).

28. J.W. Martin and R.D. Doherty, *Stability of Microstructure in Metallic Systems*, Cambridge University Press, 1976, p. 17.

Further Reading

J.M. Blakely, *Introduction to the Properties of Crystal Surfaces*, Pergamon Press, Oxford, 1973.

G.A. Chadwick and D.A. Smith (Eds.), *Grain Boundary Structure and Properties*, Academic Press, London, 1976.

H. Gleiter and B. Chalmers, 'High angle grain boundaries' in *Progress in Materials Science*, B. Chalmers, J.W. Christian and T.B. Massalski, (Eds.), Vol. 16, Pergamon, 1972.

J.W. Martin and R.D. Doherty, *Stability of Microstructure in Metallic Systems*, Cambridge University Press, Cambridge, 1976.

L.E. Murr, *Interfacial Phenomena in Metals and Alloys*, Addison-Wesley, London, 1975.

D.P. Woodruff, *The Solid–Liquid Interface*, Cambridge University Press, Cambridge, 1973.

Exercises

3.1 Use the method of Section 3.1 to estimate the surface energy of {111}, {200} and {220} surface planes in an fcc crystal. Express your answer in J/surface atom and in J/m^2.

3.2 Differentiate Equation 3.8 to obtain the slope of the $E_{SV} - \theta$ curve at $\theta = 0$.

3.3 If a two-dimensional rectangular crystal is bounded by sides of lengths l_1 and l_2 show by differentiation that the equilibrium shape is given by

$$\frac{l_1}{l_2} = \frac{\gamma_2}{\gamma_1}$$

where γ_1 and γ_2 are the energies of the sides l_1 and l_2 respectively. (The area of the crystal $l_1 l_2$ is constant.)

3.4 (a) Measure θ for the low-angle tilt boundary in Fig. 3.11.
(b) Determine the Burgers vector of the interface dislocations by making a Burgers circuit around one of the dislocations. Does the mean spacing of the dislocations agree with that predicted by Equation 3.9?

3.5 Explain why grain boundaries move towards their centre of curvature during grain growth but away from their centre of curvature during recrystallization.

3.6 (a) Suppose a recrystallized, dislocation-free grain is growing into a deformed matrix containing a dislocation density of 10^{16} m^{-2} (i.e. 10^{16} m/m^3). If the dislocations have an energy of $\mu b^2/4$ J m^{-1} calculate the pulling force acting on the recrystallized grain boundary. (Assume a shear modulus $\mu = 10^{10}$ N m^{-2} and a Burgers vector $b = 0.28$ nm.)
(b) If the recrystallized grains grow from spherically shaped nuclei, what is the diameter of the smallest nucleus that can expand into the surrounding matrix? (Assume a grain boundary energy of 0.5 J m^{-2}.)

3.7 Look up the equilibrium phase diagrams for the Al–Fe and Al–Mg systems. On the basis of these diagrams would you expect the grain boundary enrichment of Fe in dilute Al–Fe alloys to be greater or less than for Mg in dilute Al–Mg alloys at the same temperatures?

3.8 Derive Equation 3.31.

3.9 When a precipitate is surrounded by a spherical interface of radius r it is subjected to a pressure above that of the matrix by $2\gamma/r$. Consider a faceted precipitate with an equilibrium shape that of a square plate with a thickness of $2x_1$ and width $2x_2$. If the free energies of the broad faces and edges are respectively γ_1 and γ_2, show that the broad faces exert a pressure on the precipitate (ΔP) given by

$$\Delta P = 2\gamma_2/x_2$$

(Hint: consider the total force acting on the periphery of the broad faces.) Show that the same result can be obtained by considering the pressure exerted by one of the edge faces of the plate.

3.10 Explain the structure and energies of coherent, semicoherent and incoherent interfaces, with particular reference to the role of orientation relationships and misfit.

3.11 Fe-rich GP zones can form in dilute Al–Fe alloys. Given that the atomic radii are 1.43 Å for Al and 1.26 Å Fe, would you expect the zones to be spherical or disc shaped?

3.12 Mg can dissolve in Al to form a substitutional solid solution. Mg atoms are, however, bigger than Al atoms and each Mg atom therefore distorts the surrounding Al lattice, i.e. a coherency strain field effectively exists around each Mg atom. Using Equation 3.39 estimate the misfit strain energy. Express the answer in kJ mol^{-1} and eV $atom^{-1}$. (The shear modulus of Al = 25 GPa, the radius of an Al atom = 1.43 Å, the radius of a Mg atom = 1.60 Å.) What assumptions are implicit in this calculation?

3.13 Explain why fully coherent precipitates tend to lose coherency as they grow.

3.14 Show that the passage of a Shockley partial dislocation over every one of a given set of close-packed planes in fcc crystals produces a twin of the original crystal.

3.15 If the ledges on the planar semicoherent interface in Fig. 3.69 move with a transverse velocity u what will be the overall velocity of the interface